Boron Removal from Silicon Melt by gas Blowing Technique

Arman Hoseinpur^a, Stefan Andersson^b, Michael Müller^c, Kai Tang^b, Jafar Safarian^a

- a. Department of Materials Science and Engineering, Norwegian University of Science and Technology (NTNU), 7034 Trondheim, Norway.
- b. SINTEF Industry, 7465 Trondheim, Norway.
- c. Institute of Energy and Climate Research–IEK 2, Forschungszentrum Jülich GmbH, Wilhelm Johnen Straße, 52428 Jülich, Germany.

Abstract

Due to the detrimental effects of boron (B) on the efficiency of silicon photovoltaic cells, a complete boron removal from silicon is necessary to produce solar grade silicon (SoG – Si, with a maximum limit of 0.1 ppmw boron). Gas refining is a promising technique for boron removal from Si, in which the thermodynamic equilibrium never establishes. Hence, by starting from any B concertation in the melt, the required limit for SoG – Si will be achieved. This research is devoted to studying the refractory interactions' effect with melt and the chamber atmosphere on boron removal. For this purpose, gas refining experiments were carried out in alumina and graphite crucibles with H_2 and $H_2 - 3$ % H_2O refining gases. Gas refining in Ar, He, and continuous vacuuming conditions were also carried out to study the effect of chamber atmosphere. The gas refining results are supported by the characterization of the evaporated species by molecular beam mass spectroscopy (MBMS) technique. The MBMS measurements indicated the boron evaporation occurs by the formation of the volatile species BHx, BOy, B_zH_xO_v compounds. Most of these compounds were already known in literature. However, HBO, HBOH and AlBO (in the case of alumina refractories) were measured experimentally in this paper. Results indicate that the evaporation of B in the form AlBO_x compounds leads to higher mass transfer coefficients for boron removal in alumina crucibles. Density functional theory (DFT) calculations are carried out to provide a data base for the gaseous compounds in the H-B-O-Al system, including enthalpy, entropy, and C_P values for 20 compounds.

Keywords: Boron; SoG – Si; Gas refining; hydrogen; Kinetics; DFT calculations.

1.1 Introduction

Power production by photovoltaic (PV) panels has increased almost ten times over the past decade and will continue rising in the future (Wilson et al., 2020; IRENA, 2019; Yang, 2019). More than 90 % of the PV panels are produced from Si (Philips et al., 2019). The silicon for PV applications must have a purity degree of 6N (99.9999 %), known as solar grade silicon (SoG – Si). Among all the impurities that should be removed from Si to reach the SoG – Si, boron (B) is one of the most harmful elements to exist, which will reduce the efficiency of the PV modules. Boron exists in the metallurgical grade silicon (MG – Si) in tens of ppmw, while a maximum limit of 0.1 ppmw is acceptable for SoG – Si. Most metallic impurities can be removed from MG – Si through the directional solidification technique – the last key step in ingot production for solar cells. However, B has a high segregation coefficient (0.8), making it impossible to be separated from Si by the directional solidification technique. Therefore, reliable methods are required for B removal from Si.

The most important metallurgical methods investigated for B removal from Si applied till now are slag refining (Thomas et al., 2021; Safarian, 2019; Hosseinpour et al., 2019), plasma refining (Baek et al., 2017; Yvon et al., 2011; Imler et al., 2011; Nakamura et al., 2003; Alemany et al., 2002), and gas refining techniques (Sortland et al., 2014; Hui Chen et al., 2019; Jiang et al., 2019; Zhiyuan Chen et al., 2019). Slag refining is a well-established process for B removal from Si, and is industrialized by Elkem®. In slag refining, the Si melts are equilibrated with slags which absorb B from the liquid Si. Teixeira et al (Teixeira et al., 2009) reported a boron removal degree as high as almost 85 % applying SiO₂ and CaO slag system (where slag over Si weight ratio was 2.23). Jakobsson and Tangstad (Jakobsson et al., 2018; Jakobsson, 2013) reported, however, lower degrees of boron removal by the same slag system (almost 73 % for slag over Si weight ratio of unity) could be achieved in this technique. This means reaching to the SoG – Si limit depends on the initial boron content of the melt. However, in the gas refining process, the refining gases are blown over the melt surface to remove boron from liquid Si in the form of the volatile boron species such as: boron oxides (B_xO_y) , boron hydrides (BH_x) , and boron oxyhydroxides $(B_xO_vH_z)$. In the gas refining process, the thermodynamic equilibrium never establishes, and B can be continuously removed from the liquid Si. Therefore, the important advantage of the gas refining over slag refining is the independence of the gas refining process to the initial B content in the melt for reaching the SoG – Si. In addition, the slag leftover from the slag refining process is a solid waste which then imposes costs for being disposed of, especially if the environmental issues must be met in the production site. At the same time, the only by-product of the gas refining is silica fumes (SiO₂), which applications are cement and concrete production (Bayraktar, 2021; Golewski et al., 2021; Vikan et al., 2007). Plasma refining of Si is also a method resembling gas refining in terms of removing the boron species by oxidizing and removing in the form of volatile species, but totally different in physics and consuming much power in the process.

Boron removal by plasma technique was studied by Baba et al. (Baba et al., 1991) in 1991 applying water vapor and then further investigated by Nakamura et al. (Nakamura et al., 2003) and Alemany et al. (Alemany et al., 2002). Ji-jun et al. (WU et al., 2009) reported the gas

refining without plasma torch in an electric arc furnace with Ar – H₂O – O₂ gas mixtures. From 2012 the gas refining of Si by humidified hydrogen was initiated in NTNU (Nordstrand et al., 2012; Næss et al., 2012), by applying an induction furnace and top gas blowing technique. The Gas mixture of interest for the NTNU researchers has always been a combination of $H_2 - x$ % H₂O, which leads to high mass transfer coefficient values for boron removal and then higher rates of the process. When applying oxidative gases like O2 and H2O, the surface of Si melt oxidizes, and if the surface oxide layer becomes thick, then the evaporation kinetics slows down. The surface passivation of liquid silicon is studied in the oxidative plasma refining technique in (Vadon et al., 2018). A right selection of the H₂/H₂O can prevent surface oxidation, and previous studies showed the maximum process rate could be achieved when x = 3 - 4%. Safarian et al. (Safarian, Sanna, et al., 2016) compared the effect of addition of Ar and He to the H₂ – 4 % H₂O and showed that Ar addition reduces the rate of B removal while showing a better result. The mechanism of boron removal from Si is mainly known to be by the formation of $B_xO_yH_z$ compounds and among them, the HBO is known to contribute to B removal from Si more than any other compound, due to its higher vapor pressure (Altenberend et al., 2017; Safarian, Sanna, et al., 2016; Vadon et al., 2018). The following reaction is suggested for the formation of HBO:

$$\underline{\mathbf{B}} + \underline{\mathbf{H}} + \underline{\mathbf{O}} = \mathbf{HBO}_{(g)} \tag{1}$$

Where \underline{B} , \underline{H} , \underline{O} are the dissolved boron, hydrogen, and oxygen in liquid Si. The effect of the refractory—melt interaction was studied by Safarian et al. (Safarian, Tang, et al., 2016), reporting the privilege of oxide crucibles (alumina and quartz) over the graphite crucibles leading to higher rates of boron removal. When using graphite crucibles, the carbon dissolved in liquid Si will reduce the dissolved oxygen from the gas to form $CO_{(g)}$, and hence the concertation of \underline{O} is lower compared to oxide refractories (quartz and alumina). However, when comparing alumina with quartz, alumina provides higher B removal rates from liquid Si. Safarian et. al. (Safarian, Tang, et al., 2016) suggested the evaporation of boron species in the form of AlBO₂ compound in case of alumina crucibles but did not present experimental characterizations of the gas phase. The following reaction is suggested (Safarian, Tang, et al., 2016) for the formation of volatile aluminum oxyboride compound, contributing to boron removal in alumina crucibles:

$$\underline{Al} + \underline{B} + 2\underline{O} = AlBO_{2(g)}$$
 (2)

The effect of gas flow rate (for $H_2 - H_2O$ gas mixtures) and the gas stream pattern was studied by Sortland and Tangstad (Sortland et al., 2014), and Safarian et. al. (Safarian, Tang, et al., 2016), and they showed that there is a linear relationship between the gas flow rate (Q, NL/min) and the mass transfer of the boron removal (k_B , m/s) process. When doing the gas refining process by the top blowing technique, many parameters can act on the process rate such as: gas flow rate, type of gas mixture, the distance of nozzle from melt surface, diameter of the nozzle

compared to the melt surface diameters, and the melt interaction with the refractory holding liquid silicon. all of these parameters have been studied to some extent in the previous researches. Among all the variables in the gas refining of Si, we study the effect of the interaction of refractory – melt and the chamber bulk gas on the kinetics of B removal. In addition to that, the gaseous species evaporating form the melt were characterized experimentally, to expand our knowledge about the Si refining process.

2 Theoretical thermodynamics of H - Al - B - O system

In order to study the thermodynamics of the system, density-functional theory (DFT) calculations was employed by using the density functional and a maug-cc-pV(T+d)Z basis set employing the NWChem code (Valiev et al., 2010) and the thermodynamics data for the following gaseous compounds were generated:

HBO, three isomers of HBOH (H₂BO, cis-HBOH, and trans-HBOH), H₂BOH, two isomers of AlBO (AlOB and AlBO), AlBO₂, BO, BO₂, B₂O₂ BH, BH₂, BH₃, B₂O, B₂O₃, and HOBO, HB(OH)₂, B(OH)₂, B(OH)₃, B₂H₆.

In Table 1, the enthalpies of formation, standard entropies and heat capacities are given together with literature data as well as previous high-level quantum chemistry calculations using CCSD(T) (coupled cluster with single and double excitations and a perturbative treatment of triple excitations (Raghunath et al., 2013; Feller et al., 2011)) including extrapolations to the complete basis set (CBS, (Raghunath et al., 2013; Dunning et al., 2001)) limit, core-valence correlation, and relativistic corrections. For the CCSD(T) calculations the CFOUR code (Matthews et al., 2020) was used. For H₂BO, cis-HBOH, trans-HBOH, AlOB and AlBO there are no literature values of the thermodynamic quantities. In addition, the uncertainties of the literature data are very large for BH₂ and B₂O and fairly large for HBO, AlBO₂, BO, BO₂, and BH₃. In these cases it is recommended to use the calculated CCSD(T) data where available and otherwise the M06-2X data (Zhao et al., 2008). However, BO₂ has a specific electronic structure in that the electronic wavefunction has a multireference character, for which both standard DFT and coupled cluster calculations are less well suited. This, at the very least, increases the uncertainty of the results and in certain cases makes the results nontrustworthy. Since it is possible to estimate the uncertainty in the calculated enthalpy of formation of the CCSD(T) calculations for "well-behaved" systems, the CCSD(T) results for BO₂ are not included here exactly because it is not possible to make valid estimates of the uncertainty. The calculated parameters based on M062X and CCSD(T) are presented in the appendix section (Tables A-2 and A-3). By using the calculated results, the Gibbs free energy for the aforementioned gaseous compounds are calculated and presented in Figure 1. This figure indicates the boron-oxyhydrides have a negative value of Gibbs energy for formation over all the temperature ranges while the boron hydrides only get negative values of Gibbs energy at

elevated temperatures (for BH_2 and BH_3). Figure 2 also compares the results generated by M062X and CCSD(T) for some selected species.

Table 1. Thermodynamic data calculated by M06-2X, CCSD(T) [**bold** in brackets] and literature values (in parentheses: *JANAF* (italic) (Chase, 1998), others)

Molecule	ΔH _f ⁰ (298 K) / kJ/mol	S ⁰ (298 K) / J/Kmol	<i>C</i> _p (298 K) / J/Kmol
НВО	-240.18 [-238.18±5.0] (<i>-198.32±3</i> , -210.63 <i>±</i> 25 ^a)	202.40 [202.85] (<i>202.62</i> , 202.69 ^a)	34.64 [35.29] (<i>35.26</i> , 35.31 ^a)
H ₂ BO	-84.08 [-69.13±5.0]	228.20 [228.49]	41.58 [41.86]
cis-HBOH	-75.82 [-51.78±5.0]	231.82 [231.93]	40.36 [40.37]
trans-HBOH	-80.72 [- 58.68±5.0]	231.36 [231.44]	40.18 [40.14]
H₂BOH	-291.64 [-276.79±5.0] (-292.88±4.2 ^b)	230.45 [230.47]	41.90 [41.82]
AIOB	-45.19 [-27.55±6.7]	256.37 [261.83]	49.95 [50.14]
AlbO	3.99 [9.09±6.7]	251.53 [251.29]	51.14 [51.06]
AlBO ₂	-547.69 [-525.22±6.7] (<i>-541.41±17</i>)	276.92 [281.54] (<i>269.56</i>)	60.81 [61.50] (<i>66.86</i>)
ВО	-0.02 [9.55±5.0] (<i>0±8</i> , 9.81±11 ^a , 25 ^c)	203.39 [203.54] (<i>203.48</i> , 203.47 ^a , 203.5 ^c)	29.16 [29.18] (29.20, 29.20 ^a , 29.2°)
BO ₂	-284.54 (- <i>284.51±8</i> ; -309.13 <i>±</i> 20 ^a , -300.4 ^c)	230.53 (<i>229.81</i> , 230.13 ^a , 229.6 ^c)	45.21 (<i>43.28</i> , 43.28 ^a , 43.0 ^c)
ВН	442.42 [443.23±5.0] (<i>442.67±8.4</i> ; 442.7°)	171.69 [171.76] (<i>171.85</i> , 171.8 ^c)	29.11 [29.11] (29.18, 29.2°)
BH ₂	304.83 [324.25±5.0] (<i>200.83±63</i> ; 318.29±11 ^a)	194.02 [194.02] (<i>180.19</i> , 193.55 ^a)	34.70 [34.79] (<i>34.03</i> , 34.72 ^a)
BH ₃	86.00 [102.10±5.0] (<i>106.69±10</i> ; 88 <i>±</i> 10 ^a , 89.2 ^c)	188.13 [188.22] (<i>187.88</i> , 187.69 ^a , 188.2 ^c)	35.84 [35.87] (<i>36.22</i> , 34.78 ^a , 36.0 ^c)
B ₂ O	155.90 [175.77±5.9] (<i>96.23±105</i>)	241.48 [256.91] (<i>227.75</i>)	47.15 [47.32] (38.41)
B ₂ O ₂	-457.07 [-450.53±5.9] (- <i>456.81±8.4</i> ; -457.73 <i>±</i> 10 ^a : -454.8 ^c)	247.34 [248.47] (<i>242.60</i> , 249.66 ^a , 242.5 ^c)	59.08 [59.65] (<i>57.30</i> , 60.27°, 57.3°)
B ₂ O ₃	-860.46 [-836.51±5.9] (- <i>835.96±4.2</i> ; -843.8°)	284.82 [285.87] (<i>283.77</i> , 279.8°)	65.89 [66.73] (<i>66.86</i> , 66.9°)
НОВО	-562.00 [-550.98±5.0] (<i>-560.66±4.2</i> ; -561.9°)	242.34 [243.01] (<i>239.73</i> , 240.1°)	47.03 [47.43] (42.23, 42.2°)
HB(OH) ₂	-666.45 (-643.50±8.4 ^b)	255.63	55.03
B(OH) ₂	-446.03 (- <i>470±15</i>)	259.57 (<i>249.02</i>)	53.71 (52.02)
B(OH) ₃	-1026.81 (<i>-992.28±2.5</i> ; <i>-</i> 994.1°)	269.84 (<i>295.237</i>)	71.34 (65.34)
B ₂ H ₆	10.35 (41.0±16.7; 36.6±2.0°; 36.4°)	231.73 (<i>233.17</i> , 232.49 ^a , 232.1 ^c)	55.44 (<i>58.10</i> , 57.57 ^a ; 56.7 ^c)

^aGurvich et al. (Chin et al., 2004) ,^bPorter and Gupta (1964) (Porter et al., 1964) , ^cCODATA (Cox et al., 1989)).

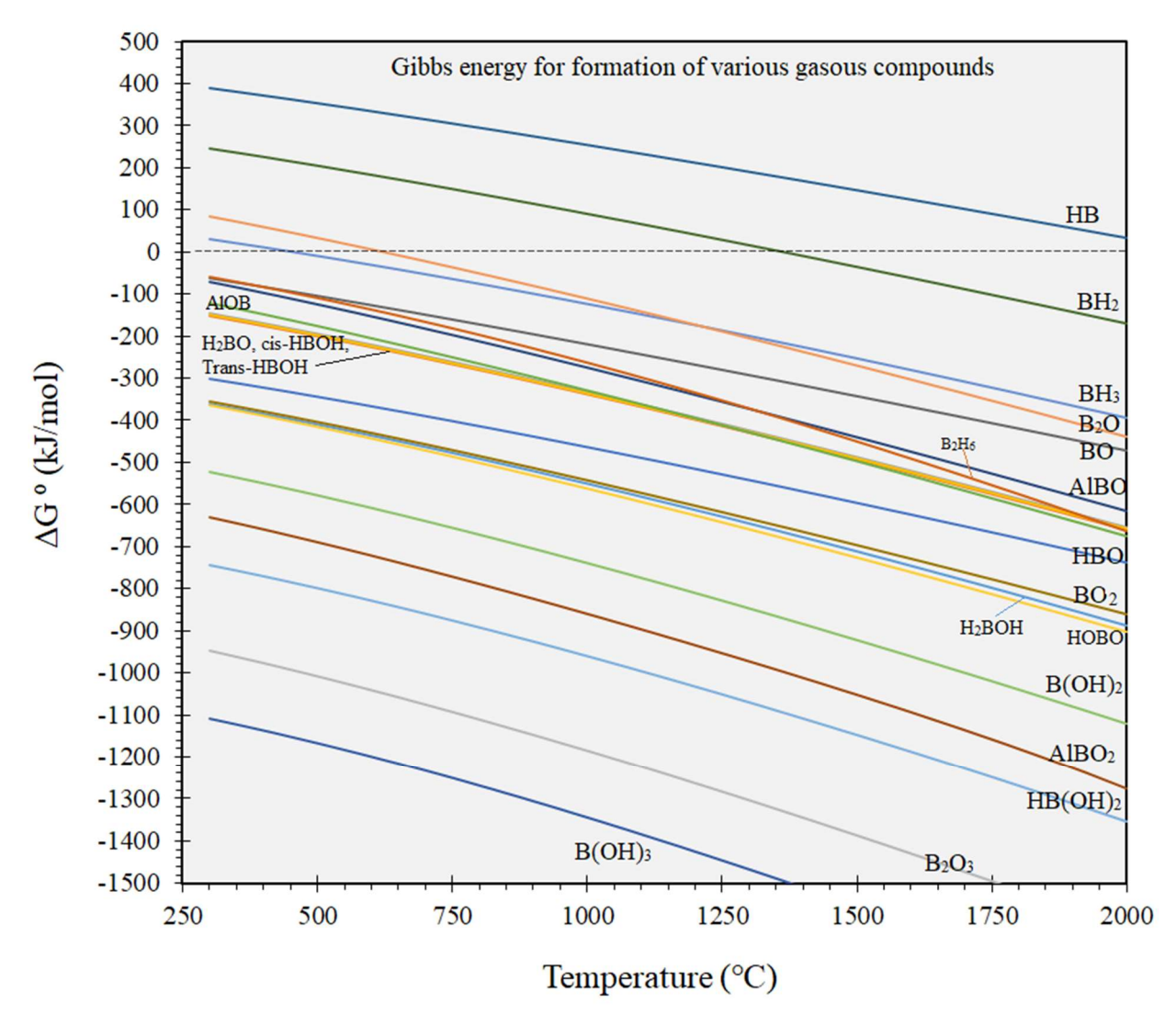


Figure 1. The Gibbs energy for formation of the gaseous compounds in H-Al-B-O system calculated by M06-2X.

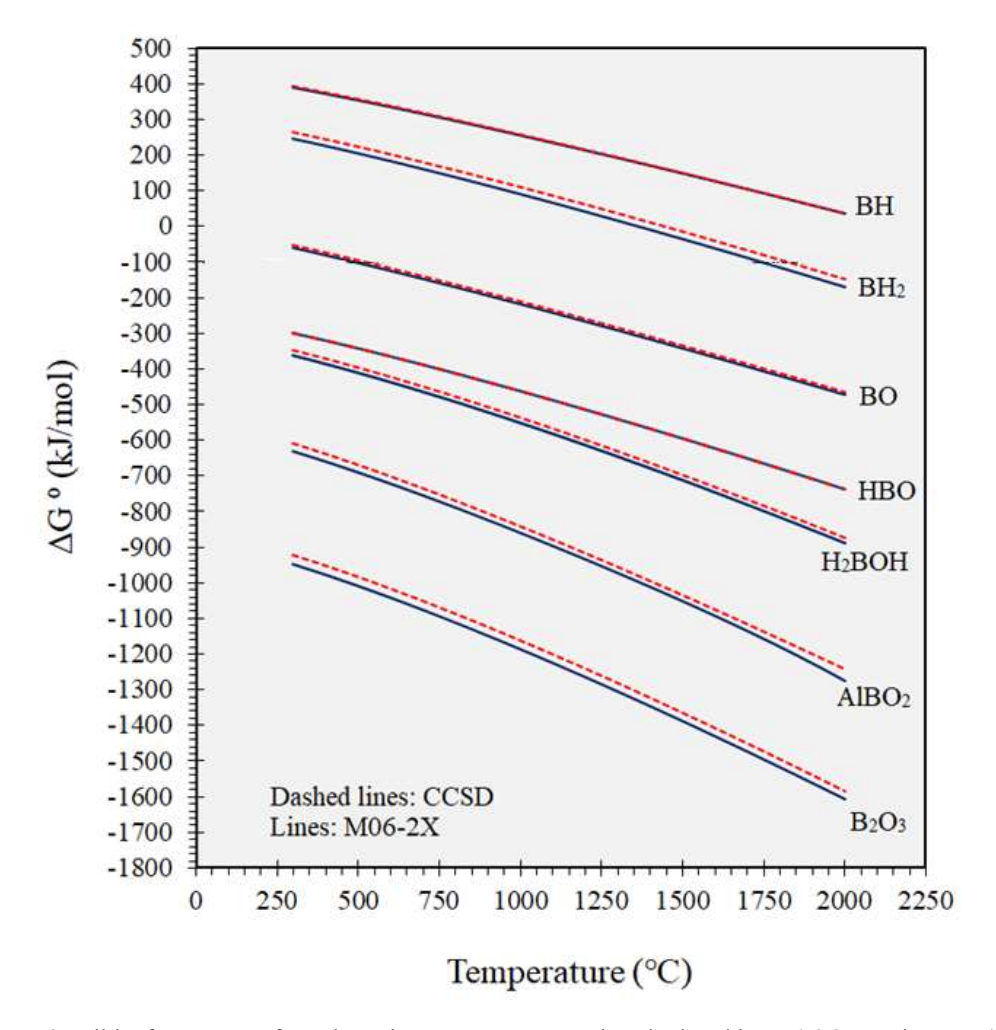


Figure 2. Gibbs free energy for selected gaseous compounds calculated by M06-2X and CCSD(T).

3 Experimental procedure

3.1 Refining experiments

In this research, all the refining experiments were carried out in a vacuum – induction furnace with the setup configuration presented in Figure 3. As shown in this figure, silicon was melted in graphite (high density, with the properties presented in (Hoseinpur et al., 2020)) or alumina sintered (ALSINT) crucibles. The crucible used for holding material was put in a bigger graphite crucible and a thermocouple type C (W – 6 % Re , W – 26 % Re, protected by an alumina sheath) was put in between of the crucibles to measure the temperature of the process. The preliminary experiments with two thermocouples, one in the inner crucible and the second one in between of the two crucibles, indicated there is only a 2 – 4 °C temperature difference, and hence the gas refining experiments were carried out with the thermocouple put in between the two crucibles. The inner crucible was charged by 213 g of Si, with a mixture of 50 wt. % of polysilicon (FBR®, 8N purity) and 50 % Silgrain® (HQ – micron cut; 0.04 wt. % Fe, 0.09 wt. % Al, 0.013 wt. % Ca, 0.001 wt. % Ti, 0.085 wt. % C, 25 ppmw P, 30 ppmw B). This

mixture provides about 15 to 20 ppmw boron impurity in the initial melt. Before the experiments, the chamber was vacuumed down to 5-7 Pa and flushed by Argon (6N) or Helium (6N) for three times. Subsequently, the power was switched on and after the material was melted, a sample was taken from the melt to record the initial composition of the melt. Then, the refining process was started by blowing the refining gas over the Si melt surface, as shown in Figure 3. Table 2 presents the experimental conditions applied for various experiments in this research. The refining gas flow was adjusted by mass flow controller (MFC) during the experiment and the gas was blown over the melt surface through a quartz lance with a 2 mm nozzle and the nozzle distance to melt surface was kept 30 mm in all the experiments. In those experiments that humidified hydrogen was used as the refining gas, the hydrogen flow was redirected to a gas humidifier unit and then was humidified with 3 % H₂O. In order to study the effect of bulk atmosphere in the furnace, in one experiment the chamber was filled with He to compare the results with the experiments where Ar was used to fill the chamber. In addition, in another experiment, the gas refining in vacuum conditions was also studied by blowing the refining gas over the melt surface while the chamber was being vacuumed continuously. In this special experiment, the pressure in the chamber was almost 5 mbar while doing the gas refining. Then, the gas blowing was started and several samples were taken from the melt during the refining process to track the boron concertation change over time. These samples were taken by quartz tubes and later were digested in a mixture of HF and HNO₃ acids, subsequently characterized by inductively plasma mass spectrometry (Agilent – 8800 ICP – MS Triple Quad). When the experiments were done, we shut down the power and let the crucible to cool down by itself. Then, some samples were taken from the fumes settled on the chamber's wall to be characterized by scanning electron microscopy (SEM).

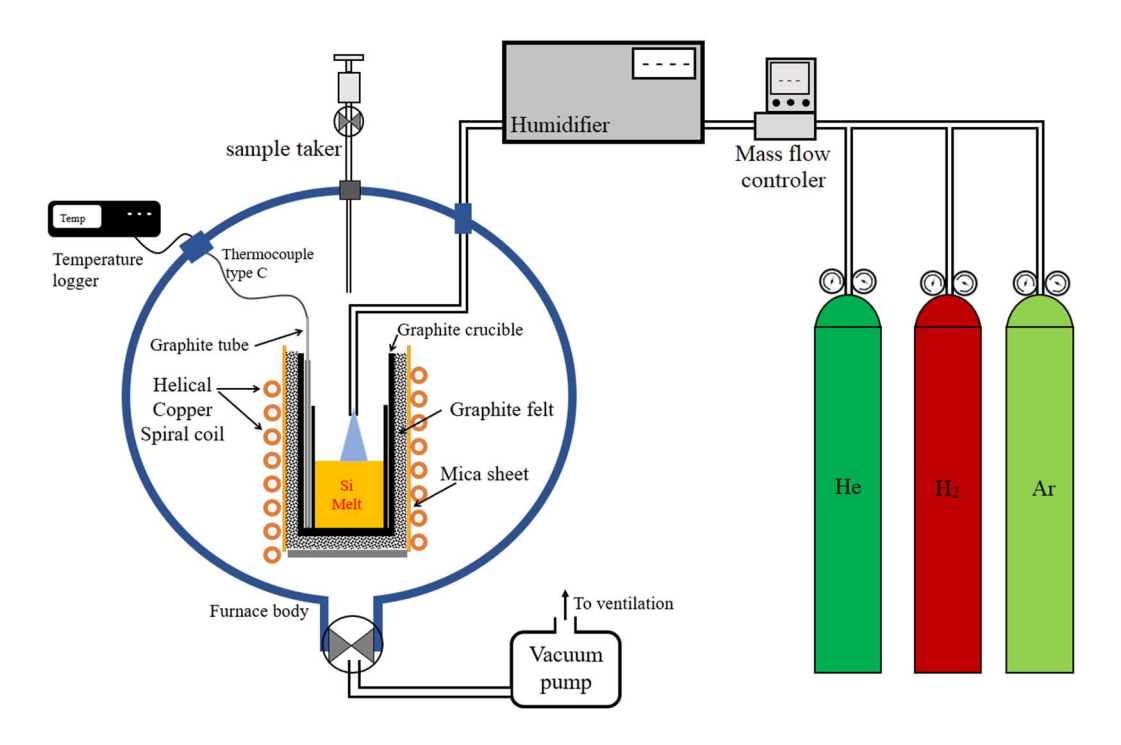


Figure 3. The schematic of the furnace and gas refining set up.

Table 2. The experimental conditions of the gas refining experiments.

Crucibles	alumina, graphite
Refining Gas	$H_2 - 3 \% H_2O / H_2O$
Gas flow rate [NL/min]	3
Chamber bulk gas atmosphere	Ar / He / vacuum
Gas nozzle diameter [mm]	2
Nozzle distance from melt surface [mm]	30
Crucible inner diameter [mm]	50 ± 1
Refining temperature [°C]	1450, 1500 , 1600

3.2 MBMS characterizations

Hot gas analysis in this study was conducted using molecular beam mass spectrometry (MBMS). A detailed description of the system used in this study is given by Wolf (Wolf et al., 2005). For all the MBMS measurements in this study, the MBMS system has been coupled to a high – temperature reactor shown schematically in Figure 4. A sample boat made of graphite, alumina or silica containing 2 grams of a Si – B (350 ppmw) was attached to the end of an alumina rod and inserted into a tubular alumina reactor with an inner diameter of 21 mm, which was housed in a high - temperature furnace. Before running the experiment, the reactor chamber was flushed by Helium gas for 10 minutes to reduce the oxygen potential in the chamber, and then the furnace was switched on. The He flow to chamber was maintained during the experiment. The furnace was maintained at a constant temperature of 1500 °C. The reactor was coupled to the sampling orifice of the MBMS device, to sample the high temperature gases. The orifice was protruded into the furnace to maintain an elevated temperature to prevent condensation of gas – phase species on the tip of the orifice. At the beginning of each experiment, the sample boat was held in the cooled zone of the reactor and a background spectrum was acquired for about 1 minute. While the MBMS was kept in a constantly scanning mode, the sample boat was inserted into the heated region of the reactor and the evaporated species were monitored over time. During experiments, 5 % H₂ in He flowed through the reactor at a flow rate of 4 normal liter per minute (NL/min). The residence time of released vapors in the reactor before sampling was about 0.1 s. Water steam was added after a few minutes via a vaporizer achieving humidity concentrations of 3-5 % in the gas stream flowing to the reactor.

Due to the relatively high gas flow necessary to minimize ambient air leaking to the reactor at the connection between furnace and MBMS, vaporization is unlikely to reach equilibrium. Therefore, the gas flow was stopped for about 20 seconds in some measurements to locally increase the concentration of vapor species above the sample boat. After switching on the gas again, high intensity peaks for qualitative analysis could be recorded. Because of this

procedure, the present results are of rather qualitative nature and therefore, released species were not quantified.

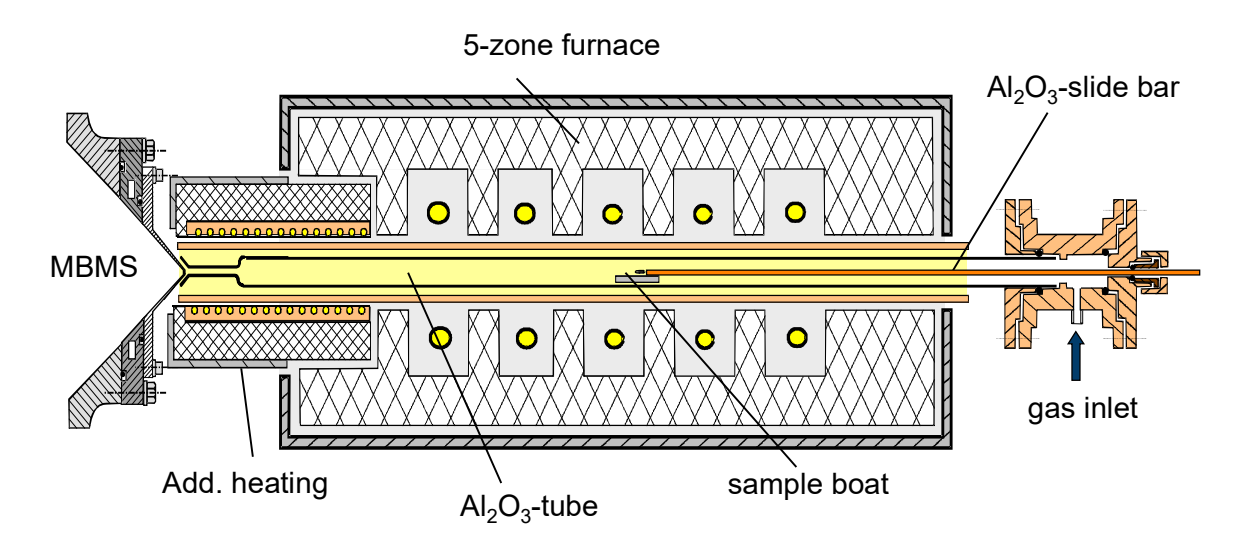


Figure 4. Setup used for vaporization experiments, from wolf et. al.(Wolf et al., 2005).

Table 3. The ions of interest studied in the MBMS and their corresponding m/z ratio.

Ion	m/z
B ⁺	10, 11
BH ⁺	11, 12
BH ₂ ⁺	12, 13
HBO ₂ ⁺	43, 44
BH ₃ ⁺	13, 14
BO ⁺	26, 27
HBO ⁺	27,28
H ¹¹ B ¹⁸ O ⁺	30
HBOH ⁺	29
B ₂ O ⁺	36, 38
BO ₂ ⁺	42, 43
$B_2O_2^+$	52, 54
AlBO ⁺	53, 54
B ₂ O ₃ ⁺	68, 70
AlBO ₂ ⁺	69, 70

The mass – to – charge ratio (m/z) range of 5 – 100 was subjected to a preliminary scan via MBMS to determine the major compounds. The ions of interest and their corresponding m/z ratio are all mentioned in the Table 3. It should be mentioned, that either ions originate from gas molecules or fragmentation within the ionization region of the MS. For example, B^+ can originate from any boron containing gas molecule. Unfortunately, not all masses could be properly recorded due to superimposing of species with the same m/z originating from background or small amounts of ambient air. For example, N_2^+ (m/z 28) superimposes BOH⁺ and Si⁺ on the same m/z. Furthermore, m/z with too high signal intensity, e.g. 44 (SiO⁺, CO₂⁺ from background) had to be excluded to prevent an overload of the multiplier.

4 Results and discussions

4.1 Rate of boron removal in gas refining experiments

The boron concertation in liquid silicon was measured by ICP – MS and all the results are presented in Table A-1 (in appendix section). To study the rate of boron removal in experimental conditions, the first-order kinetic model was applied, presented here as follows:

$$\ln\left(\frac{[\text{B wt. \%}]_0}{[\text{B wt. \%}]_t}\right) = k_B\left(\frac{A_{\text{melt surface}}}{V_{\text{melt}}}\right)t$$
 (3)

where t denotes time in seconds, the [B wt. %]₀ and [B wt. %]_t are the boron concentrations in liquid Si, at initial and also at time t, respectively. A/V is the surface to volume ratio of melt in (m⁻¹), and $k_{\rm B}$ is the overall mass transfer coefficient of boron removal in the experiments. The calculated $k_{\rm B}$ for various experimental conditions are presented in Table 4.

Table 4. The results from gas refining in various crucibles.

Experiment code	Crucible	Temperature [°C]	Chamber atmosphere	Blowing gas	k _B [μm·s ⁻¹]
1	Graphite	1500	Ar	H_2	0.9
2	Graphite	1500	Ar	$H_2 - 3 \% H_2O$	13
3	Graphite	1500	Не	$H_2 - 3 \% H_2O$	17.3
4	Graphite	1500	Vacuuming (5 mbar)	H ₂ – 3 % H ₂ O	apparent = 2.56 effective = 23.3
5	Alumina	1450	Ar	H_2	1.64
6	Alumina	1500	Ar	H_2	4.15
7	Alumina	1600	Ar	H_2	4.96
8	Alumina	1600	Ar	$H_2 - 3 \% H_2O$	15.3

Apparent: the $k_{\rm B}$ is calculated by assuming the surface of melt without impinging as the gas – melt contact area.

Effective: the $k_{\rm B}$ is calculated by assuming the surface of impinged point as the gas – melt contact area.

4.2 MBMS measurements

The results from the MBMS measurements are all presented in Figure 5. This figure represents the gaseous species that were detected in gas phase when having liquid silicon in quartz, graphite, and alumina boats. In Figure 5, the intensity of the detected species in each sample is normalized based on the sharpest peak. Figure 5(a) shows the boron species in $He - 5 \% H_2$ gas stream without any humidity added to the gas. As mentioned before, the sample was inserted into the chamber after 10 minutes of He – 5 % H₂ flushing and hence it is expected to have oxygen partially present in the chamber. From Figure 5(a) it is clear that the major boron species detected in all the samples are BH_x compounds. However, when comparing the graphite and quartz boats, it is clear that there are more B_xO_y compounds with higher intensities in case of quartz boat. As can be seen in Figure 5(a) in case of quartz boat the BO⁺₂ compound had the second highest intensity after BH₂. From Figure 5(a) it is obvious that when alumina boat is applied, the new AlBO⁺ compound is detected by MBMS, which indicates on the positive role of Si melt interaction with alumina leading to the formation of new volatile boron compounds. In addition to all the B_xH_z , $B_xH_yO_z$ and B_xO_y compounds, the B^+ ion is obvious in Figure 5(a) It is worth mentioning that boron has a very low vapor pressure (Safarian et al., 2012) and the direct evaporation of boron from silicon is not assumable. The authors have already studied the vacuum evaporation for Si having P and B concertation about 10-15 ppmw in the initial melt, and they never detected any boron evaporation even in vacuum condition. Figure 5 shows the BH_x compounds have the highest intensities while the thermodynamic calculations indicated these compounds have higher Gibbs free energy than the other boron containing species. Hence, we believe the B^+ and BH_x^+ ions detected in all cases are mainly the result of fragmentation of bigger molecules in the ionization chamber of MBMS. In addition, Figure 5(b) depicts the detected gaseous species in the gas phase when humidity (3 - 5%) was added to the gas stream. As it is obvious from this figure many of the B_xO_y peaks (in case of quartz boat) and the AlBO+ peak (in case of the alumina boat) are vanished or have lost their intensities. In the experiment with the graphite and quartz boats, it can be seen that when the humidity was added, the intensity of compound HBOH+ was increased in both cases, but the HBOH⁺ compound was detected with higher intensities in the alumina case. HBOH⁺ is detected as a new compound in this paper and previously only proved to exist by theoretical calculations (Sakai et al., 1986). It is previously discussed and shown (Safarian et al., 2014; Safarian et al., 2012) that the concertation of O is lower in graphite crucibles compared to alumina crucibles due to the formation of CO_(g), and this can explain the higher intensities of the HBOH⁺ compound detected when quartz boat was used.

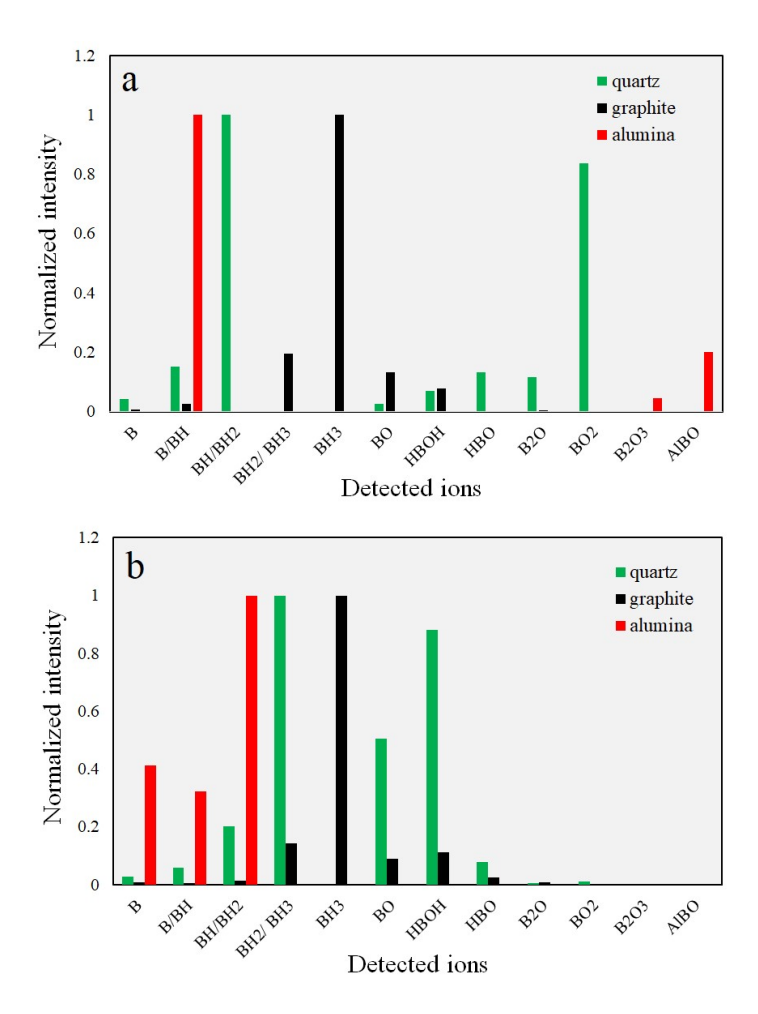


Figure 5. The measured species in MBMS results, (a): $He - 5 \% H_2$, (b): $He - 5 \% H_2$ humidified with $3 - 5 \% H_2$ O. (Detected oxide compounds in (a) is due to remained partial pressures of oxygen in chamber).

The B removal from Si melt takes place by formation of HBO compound. We can assume the formation of HBOH in gas refining through the following reaction:

$$\underline{B} + \underline{O} + 2\underline{H} = HBOH_{(g)} \tag{4}$$

However, the thermodynamics calculations presented in Figure 1 indicated that there are other molecules than HBO and HBOH having considerable negative values of Gibbs energy, such as B(OH)₃, HB(OH)₂, and B₂O₃, but none of these compounds was detected in the MBMS measurements. This could be due to the need for several elements to reach together at the melt surface and form the aforementioned molecules, which reduces the formation chance of these molecules.

Considering the discussions presented in the introduction and here, the mechanisms of B removal from liquid Si with $H_2 - H_2O$ gases is schematically summarized in Figure 6. This figure shows that an important step in the process is the dissolution of the \underline{H} and \underline{O} in the liquid Si from gas phase. When quartz and alumina crucibles are applied \underline{O} and \underline{Al} can also be dissolved from the crucibles, while in case of graphite crucibles \underline{C} will be dissolved from graphite crucible. Formation of solid silicon oxide on melt surface is also obvious on this illustration.

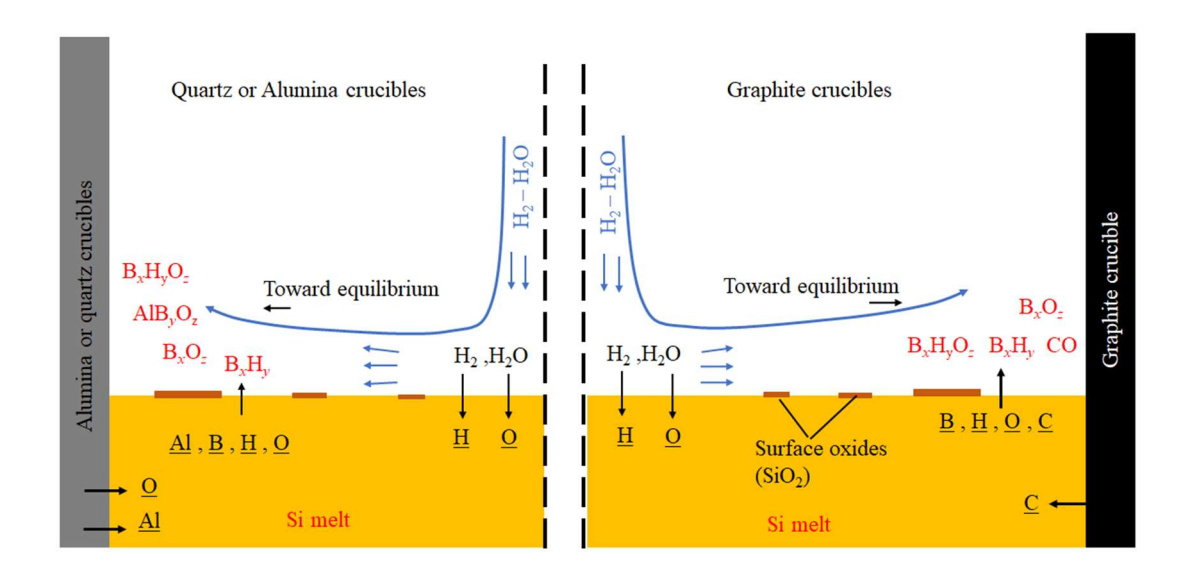


Figure 6. An illustration of the gas refining process in the quartz / alumina (left) and graphite crucibles (right), summarizing the B removal mechanisms.

4.3 Effect of crucible interactions with melt on B removal

A comparison between the experiments (1) with (2) shows, when dry hydrogen was used as the refining gas, almost, no boron removal happened from the liquid silicon. However, by the addition of humidity to hydrogen ($H_2 - 3$ % H_2O) the rate of boron removal increased from 0.9 to 13 µm/s which indicates on the important role of oxidation reactions on boron removal from liquid silicon. This indicates that the boron removal mainly takes place through the formation of $B_xH_zO_y$ species and not through the BH_z compounds, and these results are in good agreements with the findings of (Nordstrand et al., 2012; Sortland et al., 2014).

From Table 4, it is obvious that the $k_{\rm B}$ in experiment (5) is greater than experiment (1). Both experiments were carried out at 1500 °C and with dry ${\rm H}_{2(g)}$, but in alumina and graphite crucibles, respectively. These results are in good agreements with the MBMS measurements where we showed that in case of applying alumina crucibles new volatile compounds of boron like ${\rm AlBO}^+$ evaporate from melt surface, and hence the kinetics of the refining process could be accelerated in the alumina crucibles. When refining in graphite crucibles and with hydrogen gas, we can assume the boron removal with ${\rm BH}_z$ compounds, and when doing the refining process in the alumina crucibles, we can assume the removal in form of ${\rm B}_x{\rm O}_z$, ${\rm B}_x{\rm O}_z{\rm H}_y$, and ${\rm AlBO}_x$ compounds.

The effect of the temperature on boron removal in the alumina crucibles could be also studied by comparing the results obtained from experiments (5) to (7). It is obvious that an increase in temperature leads to an increased rate of the boron removal and the value of $k_{\rm B}$ increases from 1.64 to 4.15 µm/s when the temperature is increased from 1450 to 1500 °C , which is 2.5 times. However, when the temperature is increased to 1600 °C the $k_{\rm B}$ equals 4.96 µm/s. Then, beyond 1500 °C the temperature rise is no more effective for B removal. The effect of temperature is already discussed in (Safarian, Tang, et al., 2016) indicating that when temperature increases beyond 1500 °C, silicon oxidation becomes more favorable than boron oxidation reactions, leading to consuming all the dissolved oxygen in melt to form SiO_(g). In experiment (7) the humidified hydrogen (H₂ – 3 % H₂O) was applied as the refining gas and the $k_{\rm B}$ value increased to 15.3 µm/s. A comparison of the experiment (7) with experiment (8) makes it clear that when humidity is added to the refining gas, the rate of boron removal has increased almost 3 times. This indicates that however, the alumina crucibles can supply the dissolved Al and O to the melt, but the oxygen dissolved from alumina is not enough, and an exterior oxygen source is required to perform the boron removal from the liquid silicon.

In addition, the Al dissolved from alumina crucibles was also measured and is shown in Figure 7. The following reaction can be suggested for the dissolution of Al from alumina crucible:

$$Al_2O_3 = 2Al + 30 (5)$$

Figure 7 indicates that the rate of Al dissolution to the liquid Si is increases by temperature and proves when melting Si in alumina boats and crucibles, there is enough \underline{Al} in the liquid to form the AlBO_x compounds.

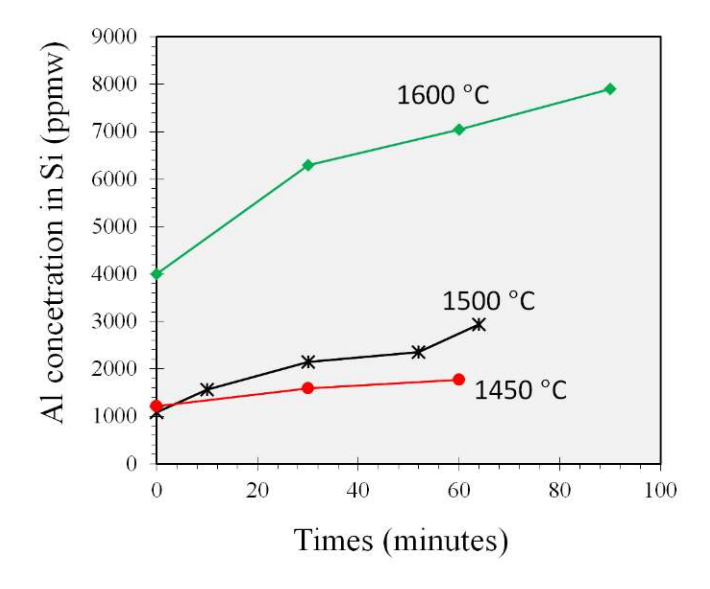


Figure 7. Aluminum concertation in liquid Si over time of gas refining.

4.4 Effect of chamber gas atmosphere

By comparing the results of experiments (2) - (4) we can study the chamber bulk gas' effect on boron removal kinetics. From Table 4 it is evident that when the chamber bulk gas is changed to He the kinetics of boron removal has accelerated and the value of $k_{\rm B}$ has increased from 13 to 17.3 µm/s, at the same temperature accounting for 33 % increase in the process rate. The positive effect of He was already reported by Safarian et al. (Safarian, Sanna, et al., 2016) and they showed when $H_2 - 4$ % H_2O is mixed with He, the mass transfer coefficient of the boron removal process is higher than when mixed with Ar. He has smaller molecules compared to Ar, with atomic radius of 0.49 and 0.88 Å, respectively. Then, assuming the same velocity for Ar and He, the momentum of Ar molecules will go higher. The Ar and He molecules will collide with the evaporated boron species from the melt surface and the higher the momentum of the foreign molecule (Ar or He), the higher chance for bouncing the boron species molecules back to the melt surface. In addition, even when the boron species are successfully evaporated, they should diffuse in the gas phase to take distance from melt surface and find their way out of the crucible, unless they may return to melt through a back reaction, and this slows down the overall process kinetics for boron removal. Obtaining the diffusion coefficient of the gaseous boron species in the gas phase is beyond the scope of this paper, but by considering the diffusion coefficient relation for gas molecules presented by Chapman and Gowling (Chapman et al., 1991), we can obtain a general view about the differences between He and Ar on the diffusion of the boron species in gas phase.

$$D_{12} \propto \frac{1}{\sigma_{12}} \sqrt{\frac{1}{m_1} + \frac{1}{m_2}} \tag{6}$$

Where D denotes the diffusion coefficient, suffixes 1 and 2 indicate gas molecule 1 and gas molecule 2, m is the mass of the molecules and σ is the average radii of the species, $\sigma_{12} = 0.5(\sigma_1 + \sigma_2)$. By assuming Ar and He as the molecule 1, and any gaseous boron compound as molecule 2, then from Equation (6) it is obvious that the higher the mass and diameter of the gas molecules the lower the diffusion of the boron species in the gas phase. Therefore, it is completely expectable for the same boron species under study to have a higher diffusion in He than Ar. In order to accelerate the diffusion of the boron species in the gas phase we carried out experiment (4), however Table 4 indicates when doing the gas refining in vacuum condition, the mass transfer coefficient for B removal has reduced to 2.56 μ m/s, which was totally opposite to our expectations. In this experiment the chamber bulk gas was continuously vacuumed during the gas refining experiment. Figure 8 compares the melt surface in the experiments (3) and (5). It is obvious from Figure 8(b) and (d) that the surface of the melt is fully impinged in case of gas blowing in vacuum condition, however, when the chamber was

in atmospheric pressure there was no significant impinging effect on the melt surface (Figure 8 (a) and (b)). Figure 8 (b) and (d) also indicate that when doing the gas refining in vacuum condition there is less amounts of condensates settled on the lance and crucible compared to Ar atmosphere, and this will further be discussed in the next section.

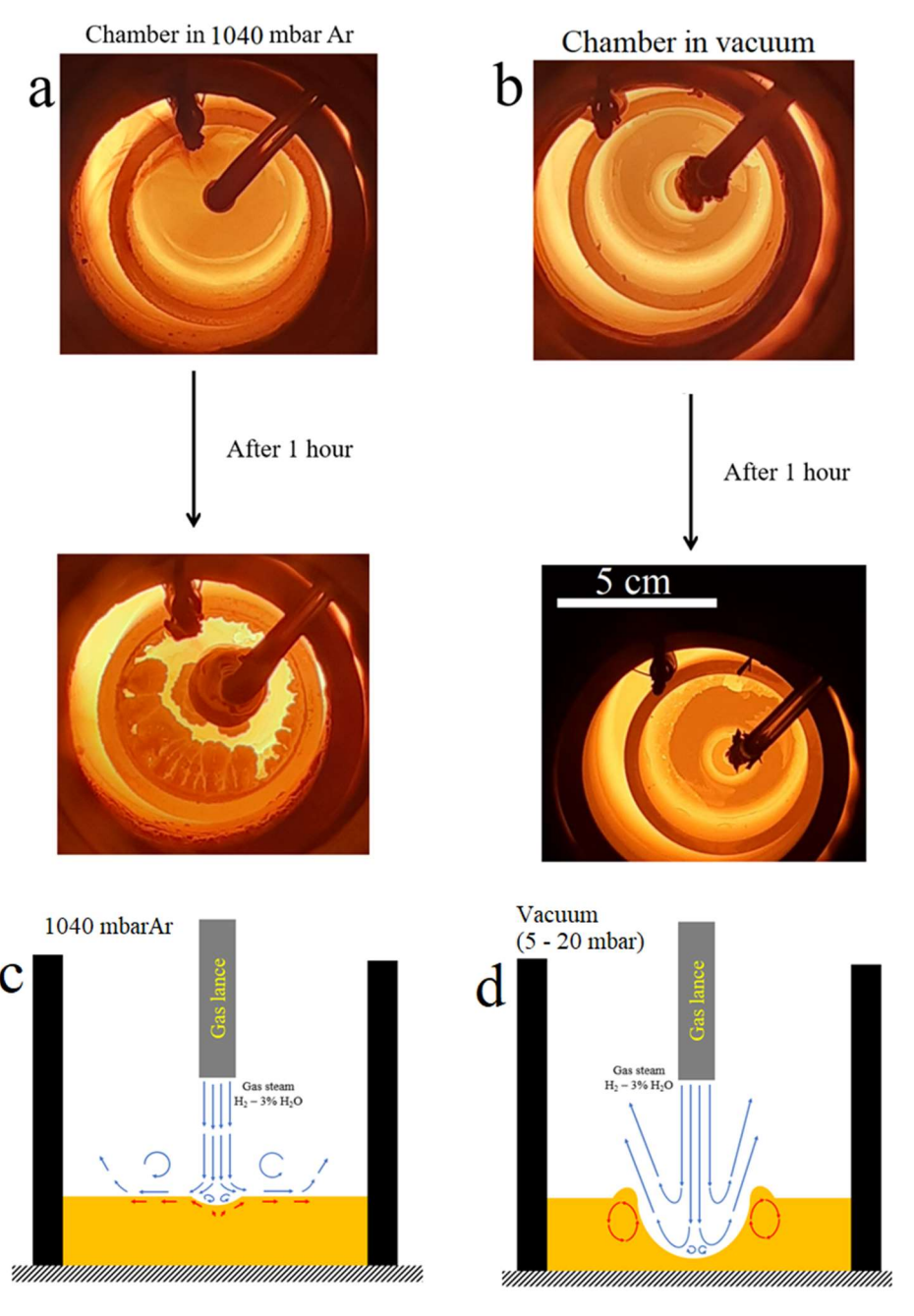


Figure 8. Photographs of the crucible during the (vacuum) refining experiments. (a) and (c): gas refining in Ar atmosphere. (b) and (d): gas refining in vacuum.

It is worth mentioning that when doing the gas refining in vacuum condition there is almost no condensates on the lance and crucible edge. The formation of the condensates on the cold parts of the crucibles and gas lance provides practical challenges in gas refining of Si. For example, as shown in Figure 8 (a), after 60 minutes of the refining process, the condensates are grown from the crucible edge toward the center of crucible, which leads to clogging the gas path toward out of the crucible, affecting on the rate of the process. The fluid dynamics for melt impinging by gas blowing is already discussed and numerically simulated in (Muñoz-Esparza et al., 2012; Nguyen et al., 2006; Standish et al., 1989) and Figure 8 (c) and (d) illustrate the gas fluid pattern when blowing in vacuum and in gas conditions. As shown in Figure 8 (c) when the gas lance is blowing in atmospheric pressure condition the gas stream spreads over the melt surface. The exact fluid dynamic of the gas blowing in experimental condition of experiment 3 is already simulated by Safarian et. al. (Safarian, Tang, et al., 2016), and the Figure 8 (c) and (d) are regenerated after their simulation results. Figure 8 (d) shows the fluid pattern of gas blowing in the vacuum condition and indicates that the gas jet makes a fully impinged point on the melt surface. In the case of vacuum condition, there is less resistance due to the low pressure of the bulk gas in the chamber and this makes the velocity of the gas jet to increase, leading to impinging the melt surface. As shown in Figure 8 (d) when the gas jet impinges the melt surface it splits and bounces back and then there is no further contact with the melt surface. As it is obvious in Figure 8 (b) the surface area of the impinged region seems to be considerably smaller than the whole melt surface area and this means that under the conditions of experiment (5), the contact area of gas and melt is smaller than for the other experiments. From the melt surface photograph presented in Figure 8 (b) the radius of impinged point (cavity) is determined as $r_{cav} = 0.00658$ m. The impinging of melt surface with gas jets is already modeled in (Visuri, Järvinen, Savolainen, et al., 2013; Visuri, Järvinen, Sulasalmi, et al., 2013) and here we can apply the following equations to calculate the depth of the cavity formed on the melt surface.

$$r_{cav} = 1.4065 \dot{M}_d^{0.282} h_{lance} \tag{7}$$

$$\dot{M}_d = \frac{m_t h_{lance}}{\rho_{Si} g h^3} (1 + \sin \theta) \tag{8}$$

$$\dot{m}_n = \frac{\dot{m}_t}{n_{lance}} \tag{9}$$

$$\dot{M}_h = \frac{\dot{m}_n \cos \theta}{\rho_{Si} g h^3} \tag{10}$$

$$h_{cav} = 4.469 \,\dot{M}_h^{0.66} h_{lance} \tag{11}$$

Where, r_{cav} is the radius of the cavity or impinged area formed on melt surface, h_{lance} is the distance if the lance tip to the melt surface. The \dot{M}_d , \dot{m}_n , \dot{M}_h , and \dot{m}_t are all dimensionless mass flow rates of the gas stream blowing out of the nozzle, and a full explanations for them could be found in (Koria et al., 1987). n_{lance} is the number of the nozzles on the gas lance tip, and it is one in this study, θ is the inclination angle of the nozzle with the lance axis, which is zero in our case, and ρ_{Si} is the density of liquid silicon. All of these parameters are shown schematically in Figure 9. By inserting the measured $r_{cav} = 0.00658$ m from Figure 8 (b) in equation (11), \dot{M}_d will be obtained, then \dot{m}_t , \dot{m}_n , \dot{M}_h will be obtained from Equations (7) -(11), respectively. Finally, from Equation ((11) h_{cav} will be calculated as 0.0298 m. The cavity with the scaled obtained dimensions is shown in Figure 7, and as it can be seen it has a half ellipse shape. Having the dimensions of the ellipse, we can calculate the impinged area's surface ($S_{impinged} = 0.5\pi h_{cav} r_{cav}$) as 2.17 E-4 m². Consequently, the effective A/V ratio is calculated as 2.713 m⁻¹. By correcting the A/V ratio in the first – order kinetic model for the experiment (4) carried out in vacuum condition, the effective $k_{\rm B}$ value obtains as 23.3 μ m/s, which is 1.79 times of that when Ar was in the chamber, and 1.34 times of the case that He was in the chamber. Therefore, the effective $k_{\rm B}$ in vacuum condition shows that when the gas atmosphere in the chamber is removed by vacuuming, the rate for the vacuum refining process increases intensively. This indicates on the important role of gas phase and is in good agreement with the result of the experiment (3), where He was used as chamber gas, providing higher diffusivities for the gas molecules.

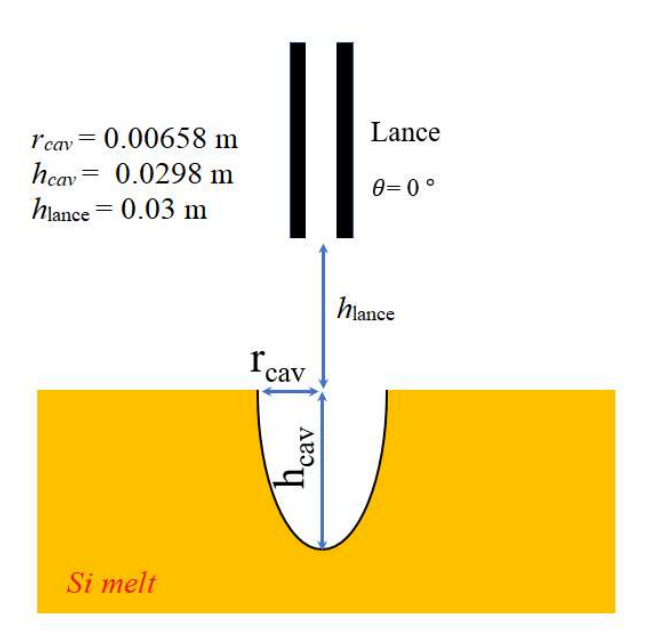


Figure 9. The calculated geometry of the impinged point on melt surface in vacuum condition, the dimensions are presented in a right scale.

4.5 Silica fume formation in gas refining

During the gas refining experiments with humidified hydrogen, $SiO_{(g)}$ forms as a product of the silicon oxidation process. The $SiO_{(g)}$ can then react with the humidity to produce small solid particles of SiO_2 and create white dust on the furnace chamber, known as silica fumes. The formation of silica fumes from the SiO gas is well discussed in the literature (Næss et al., 2012), and it could be described through the overall reaction:

$$SiO_{(g)} + H_2O_{(g)} = SiO_2 + H_{2(g)} \Delta G^{\circ}_{1500 \circ C} = -106.9 kJ$$
 (12)

The morphology of the silica fumes settled on the chamber and lance surfaces in various experiments with chamber atmosphere of Ar, He, and vacuum conditions were studied by SEM and are presented in Figure 10 and Figure 11. Figure 10 indicates a huge difference between the sizes of the fume particles in the three different experimental conditions. When He and Ar were used as the chamber bulk gas, the fume particles, settled on the chamber wall, had spherical morphology, consisted of separate spheres or several spheres attached. In addition, it is obvious from Figure 8 that the fume particles are much bigger when the chamber was filled with He gas compared to Ar and vacuum condition. The fumes settled on the chamber wall in Ar and vacuum conditions have relatively smaller sizes than in the case of He. In the case of vacuum conditions, it can be seen that some of the fume particles have grown like a comet tail. Silica fume has applications in concrete production, and the change in the morphology and size of the particles could be of interest for further study.

Figure 11 shows that the morphology of the fumes settled on the gas lance in case of the He gas is spherical but compared to the fume settled on chamber walls (Figure 10) with definitely smaller particle sizes. However, in the case of Ar gas, some tubular morphologies could be seen among the other spheres. In the case of the vacuum condition, however, the morphology of the fumes settled on the lance is totally different, and the fume is grown in the form of whiskers and columnar morphologies. We did not find any spherical particle in the sample collected from the lance of the experiment with vacuum condition, while the fume settled on the chamber wall was spherical.

Figure 12 represents the various mechanisms for the formation of silica fumes. As it is obvious from this figure, silica fumes could form in the gas phase without any preferential nucleation site or on the body of the lance, with a preferential growth direction. When forming in gas phase, small seeds could be formed in the gas and then growing equixially leading to the formation of spheres. However, if the silica fume forms by initiation on a preferential nucleation site, like the lance body, then a directionally growth will form the columnar morphologies and the whisker.

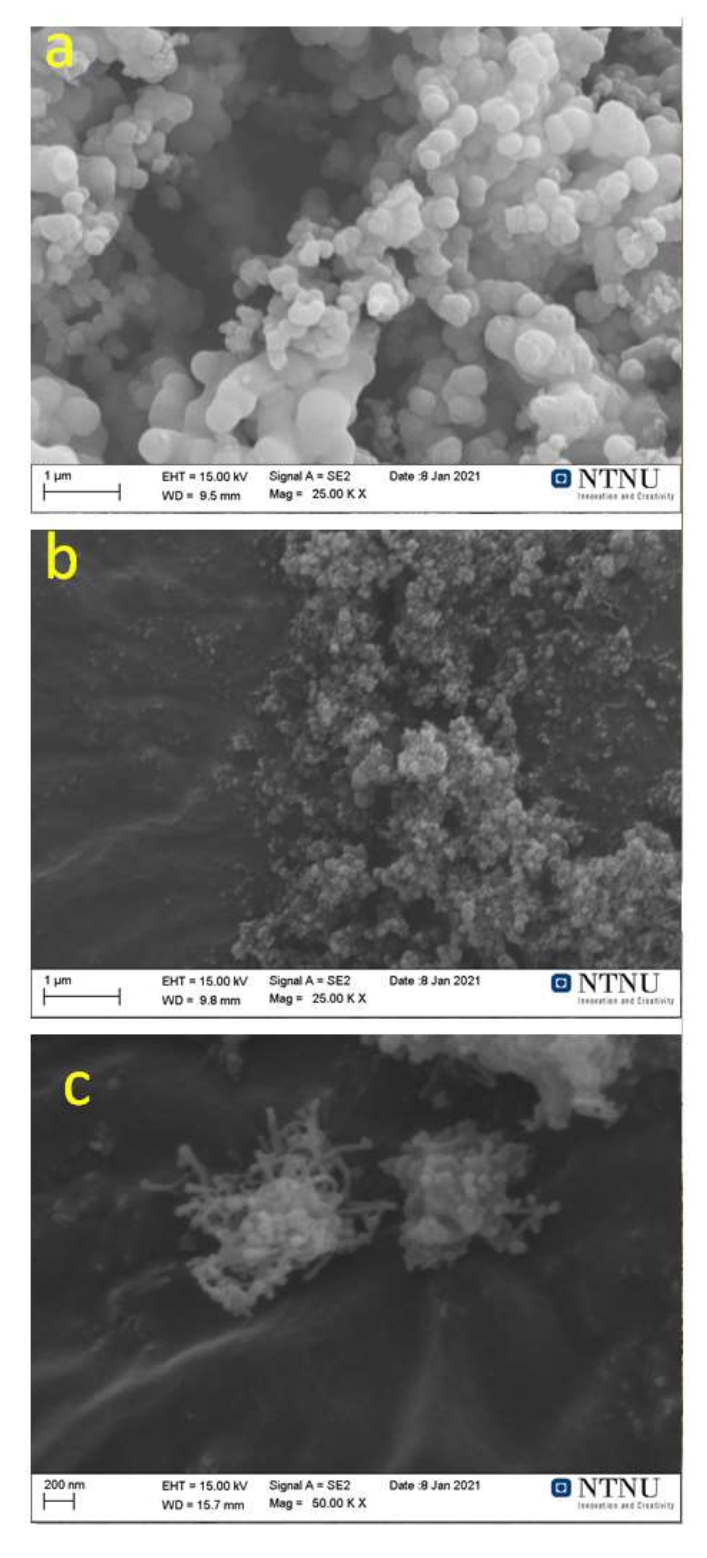


Figure 10. The SEM micrographs of the fume settled on the chamber wall, (a): He gas in the chamber, (b): Ar gas in the chamber, and (c): chamber vacuumed during the gas refining process.

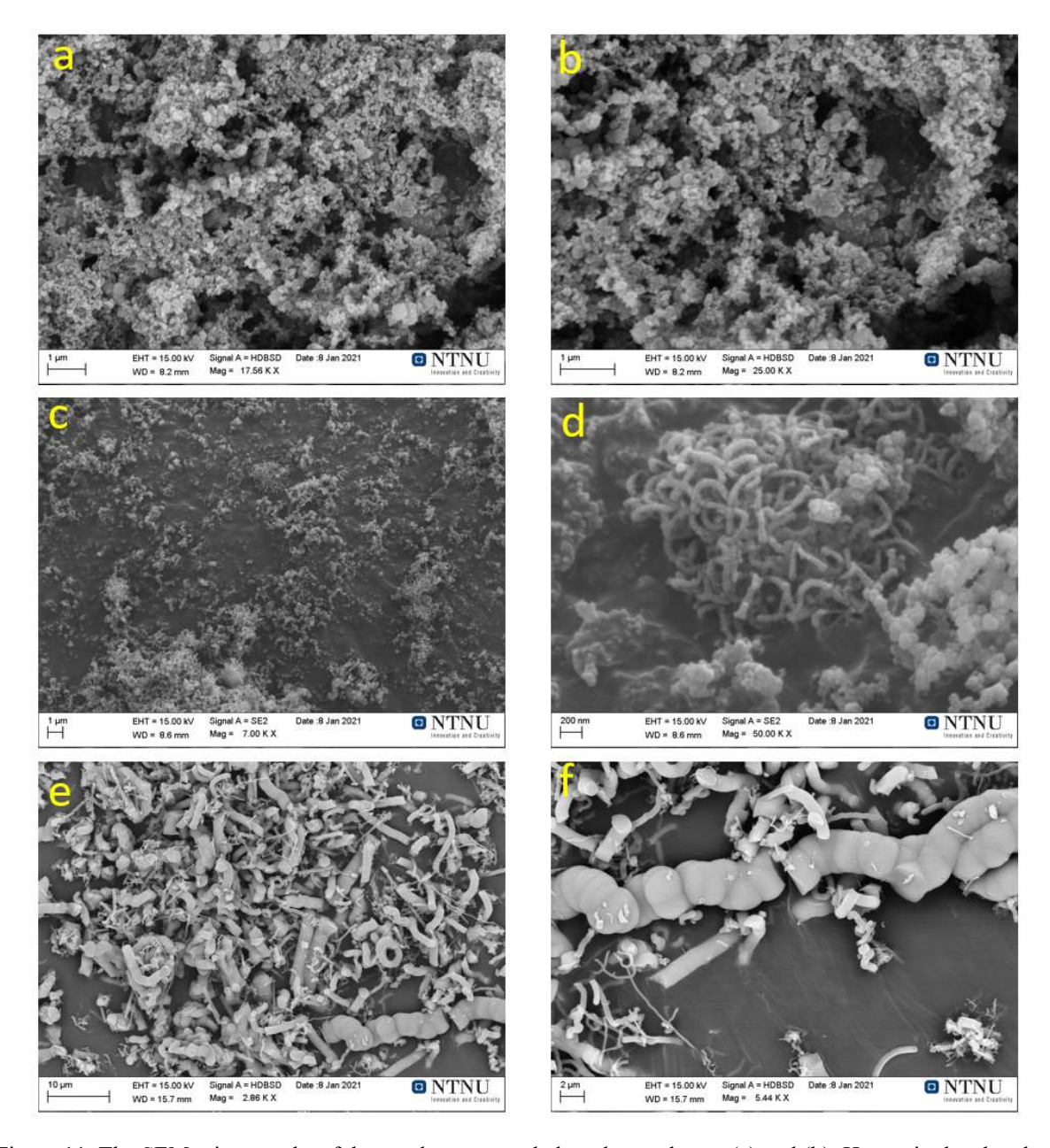


Figure 11. The SEM micrographs of the condensates settled on the gas lance, (a) and (b): He gas in the chamber, (c) and (d) Ar gas in the chamber, (e) and (f): vacuum condition.

Considering the nucleation and growth mechanisms shown in Figure 12, the differences in the morphologies detected in the fumes could be explained. The larger sizes of the spherical particles detected in case of He gas (in the sample collected from the chamber wall) is in good agreement with the previous discussion about the higher diffusivities of gaseous species in He compared to Ar. Having higher diffusivity, the gaseous species (SiO and H_2O) will reach to the surface of the seeds faster. This leads the SiO_2 seeds shown in Figure 10(a) to grow larger, before settling on the chamber wall. In the vacuum condition, however, there is lower gas density above the melt, since the chamber is being vacuumed continuously and the pressure is in the range of 5-25 mbar. Then, the seeds generated in the gas phase on top of the melt will immediately reach the chamber wall, where they settle down. Then, similar to the case of Ar,

the silica fumes in vacuum condition will have smaller sizes. In this case, further growth on the spherical particles settled on the chamber can take place, leading to the comet tail morphologies detected in Figure 10, and schematically shown in Figure 12. In addition, when doing the vacuum refining in the vacuum condition, the velocity of the gas jet flowing out of the nozzle increases intensively (Figure 8(d)). When the gas jet impinges the melt surface and bounces back, it still has high velocity and hence will carry all the silica seeds away from the melt surface and toward the chamber wall. However, the continuous gas stream over the outer surface of the gas lance provides the required gaseous reactants (SiO and H₂O) for the formation of the silica whiskers and the columns on the gas lance. The photographs of the fumes settled on the chamber wall in the two conditions vacuum and Ar atmosphere are shown Figure 13. As shown on this figure, the fumes collected from the experiment carried out in vacuum condition are fluffy while in case of Ar the fume is a fine powder.

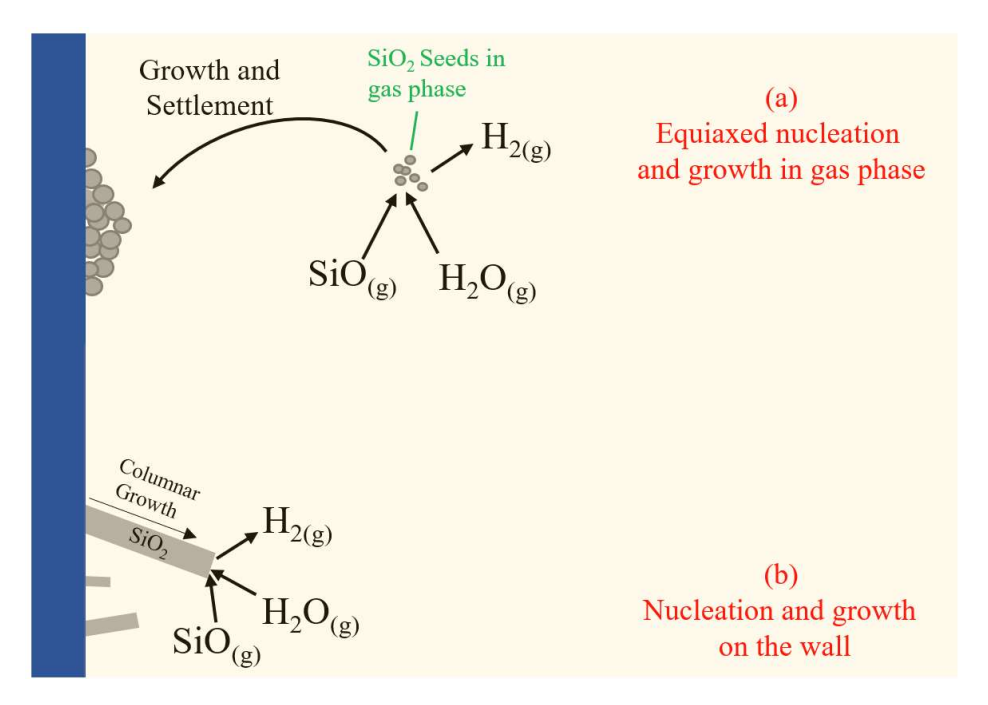


Figure 12. The schematic illustration of the silica fume formation in gas refining of Si. (a): the equiaxed growth and (b): nucleation on surface.

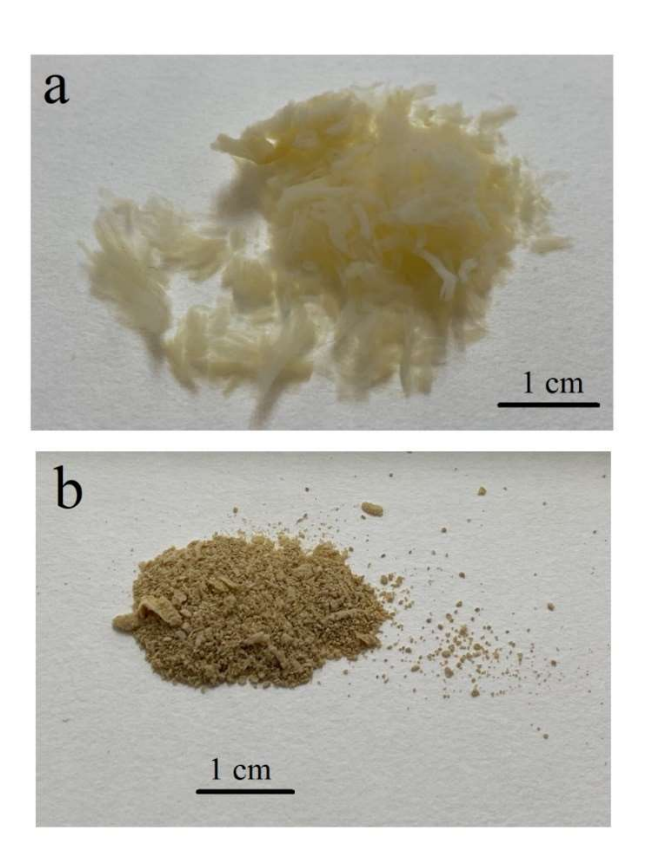


Figure 13. The photograph of the fumes collected from the chamber after gas refining. (a): in vacuum condition, (b): chamber filled with Ar gas.

5 Conclusions

Boron removal from silicon for solar applications was studied in this research. Gas refining experiments were carried out with H_2 and $H_2 - 3$ % H_2O refining gas in graphite and alumina crucibles. The MBMS was applied to characterize the off-gas of the samples in graphite, alumina, and quartz boats leading to the following remarks:

- 1. Refining experiments indicated higher rates of the boron removal process in the alumina crucibles compared to graphite.
- 2. Boron removal has 33 % higher process rate in He atmosphere compared to Ar and 79 % higher process rate when carrying out the process in vacuum condition.
- 3. MBMS measurements indicated the formation of the AlBO compound, providing higher process rates.
- 4. HBO, HBOH (in case of graphite and quartz boats) and AlBO (in case of alumina boats) were measured experimentally by MBMS technique.
- 5. Theoretical thermodynamics of the H-B-Al-O is studied by DFT calculations and the enthalpy, entropy, and C_P values for possible gaseous compounds in this system are presented.
- 6. It was shown that the morphology and size of the silica fumes can change by the chamber gas and atmospheric conditions; Silica fumes where spherical in case of Ar

and He with bigger particles sizes in the case of Ar while they had comet tail morphologies when chamber was vacuumed during gas refining.

Acknowledgments

This research was financed by the Norwegian University of Science and Technology (NTNU) and was done in cooperation with the Research Center for Sustainable Solar Cell Technology (FME SuSolTech) in Norway and the institute for energy and climate research (IEK-2), Forschungszentrum Jülich in Germany. The support from Elkem® Bremanger for silicon material is highly acknowledged. The gas refining experiments done by the vacuum induction furnace were all carried out in NTNU and the hot gas characterizations by MBMS were carried out in Forschungszentrum Jülich. The authors' appreciations go to Dr. Lars Klemet Jakobsson from Elkem® in Kristiansand for his kind comments on the manuscript.

Appendix

Table A1 shows the concentration of B measured by ICP – MS at various times during the gas refining process. In Table A2 and Table A3, fits to the calculated thermodynamic quantities are presented, based on the M06-2X and CCSD(T) calculations, respectively. The parameters (a_1, a_2, \ldots, a_7) are for the NASA polynomial functional form as:

$$\frac{c_p}{R} = a_1 + a_2 T + a_3 T^2 + a_4 T^3 + a_5 T^4 \tag{A-1}$$

$$\frac{H}{RT} = a_1 + a_2 \frac{T}{2} + a_3 \frac{T^2}{3} + a_4 \frac{T^3}{4} + a_5 \frac{T^4}{5} + \frac{a_6}{T}$$
(A-2)

$$\frac{s}{R} = a_1 \ln T + a_2 T + a_3 \frac{T^2}{2} + a_4 \frac{T^3}{3} + a_5 \frac{T^4}{4} + a_7 \tag{A-3}$$

The parameters are given for fits in two temperature ranges: 298-1000 K and 1000-3500 K.

Table A-1. The concertation of boron measured by ICP-MS at various times during the gas refining.

Experiment Number and Conditions	Refining time (t, minutes) and B concertation (CB, ppmw)						
1 (Graphite , H2 in Ar. 1500 °C)	t = 0 CB =15.70	t = 10 CB =15.64	t = 33 CB =14.59	t = 50 CB =14.62			
2 (Graphite , H2 – 3 % H2O in Ar, 1500 °C)	t = 0 CB = 9.21	t = 40 CB =3.82	t = 78 CB =2.32	t = 98 CB =1.32			
3 (Graphite, H2 – 3 % H2O in He, 1500 °C)	t = 0 CB =11.77	t = 30 CB =6.65	t = 65 CB =2.1	t = 100 CB =0.9			
4 (Graphite, H2 – 3 % H2O in vacuum, 1500 °C)	t = 0 CB =11.85	t = 30 CB =10.95	t = 55 CB =9.44				
5 (Alumina, H2 in Ar, 1450 °C)	t = 0 CB = 17.18	t = 30 CB =15.38	t = 60 CB = 14.70				
6 (Alumina , H2 in Ar, 1500 °C)	t = 0 CB = 17.07	t = 10 CB =16.00	t = 30 CB = 13.14	t = 52 CB =12.10	t = 62 CB = 10.33		
7 (Alumina, H2 in Ar, 1600 °C)	t = 0 CB = 14.70	t = 30 CB =10.07	t = 60 CB = 9.26	t = 90 CB =7.75	t = 120 CB = 6.3		
8 (Alumina, H2 – 3 % H2O, in Ar, 1500 °C)	t = 0 CB = 17.44	t = 20 CB =10.62	t = 60 CB = 3.59				

Table A-2. Thermodynamic data (based on M06-2X calculations) as parameters for NASA polynomials.

	a ₁	a ₂	a ₃	a ₄	a ₅	a ₆	a ₇
НВО		_	-		_	<u> </u>	
298-1000 K	2.192686E+0 0	9.051491E-03	-1.007469E- 05	7.108782E-09	-2.160175E- 12	-2.986665E+04	9.540324E+0 0
1000-3500 K	3.214183E+0 0	4.641432E-03	-2.175393E- 06	4.850579E-10	-4.192093E- 14	-3.008395E+04	4.622818E+0 0
H₂BO							
298-1000 K	2.338867E+0 0	1.080959E-02	-6.917617E- 06	2.005208E-09	-1.285423E- 13	-1.123348E+04	1.118782E+0 1
1000-3500 K	3.741728E+0 0	7.102868E-03	-3.447383E- 06	7.891389E-10	-6.958257E- 14	-1.164750E+04	3.859177E+0 0
cis-HBOH							
298-1000 K	2.032732E+0 0	1.168748E-02	-8.077930E- 06	1.819725E-09	3.526881E- 13	-1.017678E+04	1.315776E+0 1
1000-3500 K	3.962777E+0 0	5.961031E-03	-2.616845E- 06	5.570540E-10	-4.657031E- 14	-1.066841E+04	3.341731E+0 0
trans-HBOH							
298-1000 K	2.034096E+0 0	1.148565E-02	-7.475187E- 06	1.115573E-09	6.298503E- 13	-1.076126E+04	1.313388E+0 1
1000-3500 K	3.989144E+0 0	5.854720E-03	-2.544610E- 06	5.377842E-10	-4.472614E- 14	-1.126497E+04	3.155367E+0 0
H₂BOH							
298-1000 K	1.551882E+0 0	1.228854E-02	3.693286E-08	-8.297778E- 09	4.112447E- 12	-3.607081E+04	1.527393E+0 1
1000-3500 K	3.407264E+0 0	9.881576E-03	-4.487463E- 06	9.807335E-10	-8.366881E- 14	-3.669478E+04	5.082490E+0 0
AIOB							
298-1000 K	4.888103E+0 0	4.581050E-03	-2.877943E- 06	2.602405E-10	2.611103E- 13	-7.071663E+03	1.742569E+0 0
1000-3500 K	5.970225E+0 0	1.941380E-03	-1.017948E- 06	2.462068E-10	-2.260333E- 14	-7.393681E+03	- 3.947136E+0 0
AIBO							
298-1000 K	5.307458E+0 0	4.067187E-03	-5.387294E- 06	4.707208E-09	-1.701416E- 12	-1.243850E+03	-9.993693E- 01
1000-3500 K	5.715965E+0 0	2.113971E-03	-1.056673E- 06	2.469242E-10	-2.209826E- 14	-1.339847E+03	- 2.965471E+0 0
AIBO ₂							
298-1000 K	3.791587E+0 0	1.754482E-02	-2.389140E- 05	1.727192E-08	-5.096931E- 12	-6.760326E+04	7.391040E+0 0
1000-3500 K	7.239279E+0 0	3.995178E-03	-2.046909E- 06	4.872488E-10	-4.422530E- 14	-6.837202E+04	- 9.465359E+0 0
ВО							
298-1000 K	3.871990E+0 0	-2.985725E- 03	7.619758E-06	-6.277562E- 09	1.804076E- 12	-1.079853E+03	3.004375E+0 0
1000-3500 K	2.878687E+0 0	1.897566E-03	-9.394715E- 07	2.179074E-10	-1.938733E- 14	-9.342059E+02	7.553180E+0 0
BO ₂							
298-1000 K	1.889568E+0 0	1.825942E-02	-2.642680E- 05	1.861302E-08	-5.177116E- 12	-3.539771E+04	1.253626E+0 1
1000-3500 K	6.059342E+0 0	1.902560E-03	-1.023704E- 06	2.520001E-10	-2.342658E- 14	-3.630803E+04	- 7.752557E+0 0
ВН						1	
298-1000 K	3.692089E+0 0	-1.295861E- 03	2.470678E-06	-8.474909E- 10	-1.187262E- 13	5.214727E+04	-1.020868E- 01
1000-3500 K	2.681248E+0 0	1.926903E-03	-8.820968E- 07	1.923252E-10	-1.628899E- 14	5.238393E+04	4.962222E+0 0

BH ₂							
298-1000 K	3.573760E+0 0	2.255645E-03	-1.291981E- 06	1.869105E-09	-9.248958E- 13	3.550450E+04	2.343090E+0 0
1000-3500 K	2.617657E+0 0	4.453314E-03	-1.972256E- 06	4.188262E-10	-3.473053E- 14	3.577305E+04	7.350889E+0 0
BH₃							
298-1000 K	3.507845E+0 0	-4.731541E- 05	1.267547E-05	-1.315187E- 08	4.349392E- 12	9.211329E+03	2.199403E+0 0
1000-3500 K	1.813296E+0 0	8.772426E-03	-4.069795E- 06	8.992461E-10	-7.711064E- 14	9.450423E+03	9.880622E+0 0
B ₂ O							
298-1000 K	5.125271E+0 0	9.296838E-05	8.772230E-06	-1.124201E- 08	4.265168E- 12	1.716147E+04	-4.846355E- 01
1000-3500 K	5.549808E+0 0	2.490519E-03	-1.311315E- 06	3.180760E-10	-2.926215E- 14	1.686821E+04	- 3.553158E+0 0
B ₂ O ₂							
298-1000 K	3.792476E+0 0	1.740691E-02	-2.721236E- 05	2.297527E-08	-7.645158E- 12	-5.667889E+04	3.971579E+0 0
1000-3500 K	6.390474E+0 0	4.833182E-03	-2.404358E- 06	5.600885E-10	-5.001756E- 14	-5.717459E+04	- 8.231215E+0 0
B ₂ O ₃							
298-1000 K	2.814090E+0 0	2.561257E-02	-3.565608E- 05	2.698822E-08	-8.319591E- 12	-1.052014E+05	1.194845E+0 1
1000-3500 K	7.395180E+0 0	6.734240E-03	-3.403456E- 06	8.022708E-10	-7.229531E- 14	-1.061972E+05	- 1.027722E+0
НОВО							
298-1000 K	2.152567E+0 0	1.703298E-02	-2.179824E- 05	1.496985E-08	-4.150940E- 12	-3.630995E+04	1.264842E+0
1000-3500 K	5.244871E+0 0	4.536541E-03	-1.944264E- 06	4.071948E-10	-3.367186E- 14	-3.695483E+04	- 2.318121E+0 0
HB(OH) ₂							
298-1000 K	1.734973E-02	2.932618E-02	-2.767929E- 05	1.226846E-08	-1.688567E- 12	-8.124362E+04	2.302803E+0 1
1000-3500 K	5.945754E+0 0	9.676424E-03	-4.180178E- 06	8.814966E-10	-7.331603E- 14	-8.265630E+04	- 6.632140E+0
B(OH) ₂							,
298-1000 K	1.287905E+0 0	2.410929E-02	-2.689617E- 05	1.493284E-08	-3.129964E- 12	-5.489053E+04	1.776234E+0
1000-3500 K	6.322698E+0 0	5.936437E-03	-2.390473E- 06	4.752730E-10	-3.768453E- 14	-5.601149E+04	- 7.050924E+0 0
В(ОН)3							
298-1000 K	-8.567872E- 01	4.568938E-02	-5.703717E- 05	3.594749E-08	-8.891439E- 12	-1.248345E+05	2.594829E+0 1
1000-3500 K	8.739200E+0 0	9.130390E-03	-3.690762E- 06	7.378861E-10	-5.887490E- 14	-1.268972E+05	- 2.092446E+0 1
B ₂ H ₆							
298-1000 K	3.771767E-01	2.192913E-02	7.654154E-08	-1.131216E- 08	4.939286E- 12	1.770757E+02	1.926986E+0
1000-3500 K	2.200759E+0 0	2.246729E-02	-1.090734E- 05	2.497568E-09	-2.202619E- 13	-6.746032E+02	8.313307E+0 0

Table A-3. Thermodynamic data (based on CCSD(T) calculations) as parameters for NASA polynomials.

	a ₁	a ₂	a ₃	a ₄	a ₅	a ₆	a ₇
HBO							
298-1000 K	2.204674E+0 0	9.511337E-03	-1.111546E- 05	8.031437E-09	-2.461458E- 12	- 2.973189E+0 4	9.427524E+0 0
1000-3500 K	3.350674E+0 0	4.516351E-03	-2.125080E- 06	4.752700E-10	-4.117008E- 14	- 2.997224E+0 4	3.924689E+0 0
H ₂ BO							
298-1000 K	2.398786E+0 0	1.068061E-02	-6.758193E- 06	1.971156E-09	-1.555221E- 13	- 9.448668E+0 3	1.091219E+0 1
1000-3500 K	3.781941E+0 0	7.102937E-03	-3.463388E- 06	7.954741E-10	-7.031671E- 14	- 9.864376E+0 3	3.658347E+0 0
cis-HBOH							
298-1000 K	2.010623E+0 0	1.177298E-02	-8.074977E- 06	1.730109E-09	3.970424E-13	- 7.282468E+0 3	1.327190E+0 1
1000-3500 K	3.979889E+0 0	5.981595E-03	-2.639650E- 06	5.642779E-10	-4.733128E- 14	- 7.787455E+0 3	3.241731E+0 0
trans-HBOH							
298-1000 K	2.013771E+0 0	1.151420E-02	-7.339242E- 06	9.032882E-10	7.158498E-13	- 8.107052E+0 3	1.324632E+0 1
1000-3500 K	3.991013E+0 0	5.895086E-03	-2.577275E- 06	5.472420E-10	-4.568047E- 14	- 8.620708E+0 3	3.134805E+0 0
H ₂ BOH							
298-1000 K	1.547553E+0 0	1.216517E-02	5.124492E-07	-8.789351E- 09	4.278505E-12	- 3.428123E+0 4	1.532063E+0 1
1000-3500 K	3.390419E+0 0	9.968311E-03	-4.550637E- 06	9.984243E-10	-8.542722E- 14	3.491191E+0	5.147095E+0 0
AlOB							
298-1000 K	4.920185E+0 0	4.483624E-03	-2.540733E- 06	-1.751085E- 10	4.411304E-13	- 4.957617E+0 3	2.234465E+0 0
1000-3500 K	6.023645E+0 0	1.881659E-03	-9.894724E- 07	2.398008E-10	-2.204734E- 14	5.288261E+0 3	- 3.584142E+0 0
AlbO							
298-1000 K	5.278695E+0 0	4.016536E-03	-4.785272E- 06	3.875755E-09	-1.366362E- 12	- 6.237499E+0 2	-8.694788E- 01
1000-3500 K	5.769408E+0 0	2.080851E-03	-1.051079E- 06	2.475126E-10	-2.227909E- 14	- 7.528781E+0 2	- 3.316339E+0 0
AlBO ₂							
298-1000 K	3.945705E+0 0	1.717656E-02	-2.332997E- 05	1.681781E-08	-4.954623E- 12	- 6.493380E+0 4	7.157441E+0 0
1000-3500 K	7.347670E+0 0	3.879522E-03	-1.993551E- 06	4.755260E-10	-4.322536E- 14	- 6.569610E+0 4	- 9.493774E+0 0
ВО							
298-1000 K	3.884928E+0 0	-3.201944E- 03	8.507345E-06	-7.339146E- 09	2.209619E-12	7.045289E+0 1	2.982897E+0 0
1000-3500 K	2.940350E+0 0	1.854292E-03	-9.287805E- 07	2.173253E-10	-1.946645E- 14	1.890463E+0 2	7.208263E+0 0
ВН	_		_			_	

298-1000 K	3.713848E+0	-1.477944E-	2.971175E-06	-1.338830E-	4.552086E-14	5.224325E+0	-1.822718E-
	0	03		09		4	01
1000-3500 K	2.693290E+0	1.938478E-03	-8.967747E-	1.972295E-10	-1.682423E-	5.247342E+0	4.888887E+0
	0		07		14	4	0
BH ₂							
298-1000 K	3.558525E+0	2.406046E-03	-1.587764E-	2.155872E-09	-1.032333E-	3.784084E+0	2.396170E+0
	0		06		12	4	0
1000-3500 K	2.637682E+0	4.463811E-03	-1.988762E-	4.244878E-10	-3.535214E-	3.809991E+0	7.227696E+0
	0		06		14	4	0
BH₃							
298-1000 K	3.529327E+0	-2.150277E-	1.314701E-05	-1.356482E-	4.465672E-12	1.114532E+0	2.119366E+0
	0	04		08		4	0
1000-3500 K	1.821523E+0	8.831680E-03	-4.122229E-	9.151737E-10	-7.877142E-	1.137521E+0	9.813695E+0
	0		06		14	4	0
B ₂ O							
298-1000 K	5.210220E+0	-2.958266E-	9.518793E-06	-1.189647E-	4.480348E-12	1.953675E+0	9.747341E-01
	0	04		08		4	
1000-3500 K	5.562765E+0	2.474265E-03	-1.302851E-	3.160382E-10	-2.907563E-	1.925514E+0	-
	0		06		14	4	1.763733E+0
							0
B ₂ O ₂							
298-1000 K	4.042288E+0	1.610861E-02	-2.408586E-	1.990104E-08	-6.582318E-	-	2.957229E+0
	0		05		12	5.593133E+0	0
						4	
1000-3500 K	6.536833E+0	4.727580E-03	-2.375651E-	5.574733E-10	-5.005675E-	-	-
	0		06		14	5.644265E+0	8.932933E+0
						4	0
B_2O_3							
298-1000 K	2.973091E+0	2.521099E-02	-3.470911E-	2.599687E-08	-7.963295E-	-	1.125446E+0
	0		05		12	1.023566E+0	1
						5	
1000-3500 K	7.579366E+0	6.562628E-03	-3.334145E-	7.888628E-10	-7.128083E-	-	-
	0		06		14	1.033735E+0	1.117347E+0
						5	1
НОВО							
298-1000 K	2.295688E+0	1.643733E-02	-2.058085E-	1.387339E-08	-3.790272E-	-	1.204597E+0
	0		05		12	6.752667E+0	1
						4	
1000-3500 K	5.297016E+0	4.509779E-03	-1.941185E-	4.079875E-10	-3.383282E-	-	-
	0		06		14	6.816239E+0	2.529394E+0
						4	0

References

- Alemany, C., Trassy, C., Pateyron, B., Li, K.-I. and Delannoy, Y., Refining of Metallurgical-Grade Silicon by Inductive Plasma, *Solar Energy Materials and Solar Cells*, vol. **72**, no. 1–4, pp. 41–48, April 2002. DOI: 10.1016/S0927-0248(01)00148-9
- Altenberend, J., Chichignoud, G. and Delannoy, Y., Study of Mass Transfer in Gas Blowing Processes for Silicon Purification, *Metallurgical and Materials Transactions E*, vol. **4**, no. 1, pp. 41–50, March 23, 2017. DOI: 10.1007/s40553-016-0105-x
- Baba, H., Yuge, N., Sakaguchi, Y., Fukai, M., Aratani, F. and Habu, Y., Removal of Boron from Molten Silicon by Argon-Plasma Mixed with Water Vapor, in *Tenth E.C. Photovoltaic Solar Energy Conference*, Dordrecht: Springer Netherlands, pp. 286–89, 1991.
- Baek, S. H., Lee, H., Min, D. J., Choi, S. J., Moon, B. M. and Jung, H. Do, Novel Recycling Method for Boron Removal from Silicon by Thermal Plasma Treatment Coupled with Steam and Hydrogen Gases, *Metals*, vol. 7, no. 10, 2017. DOI: 10.3390/met7100401
- Bayraktar, O. Y., Possibilities of Disposing Silica Fume and Waste Glass Powder, Which Are Environmental Wastes, by Using as a Substitute for Portland Cement, *Environmental Science and Pollution Research*, 2021. DOI: 10.1007/s11356-020-12195-9
- Chapman, S. and Cowling, T. G., The Mathematical Theory of Non-Uniform Gases, D. Burnet, Ed., Cambridge University Press, pp. 93–96, 1991.
- Chase, M. W., NIST-JANAF Hermochemical Tables, J. Phys. Chem. Ref. Data Monogr., vol. 9, p. 1, 1998.
- Chen, H., Yuan, X., Morita, K., Zhong, Y., Ma, X., Chen, Z. and Wang, Y., Reaction Mechanism and Kinetics of Boron Removal from Molten Silicon via CaO-SiO2-CaCl2 Slag Treatment and Ammonia Injection, *Metallurgical and Materials Transactions B: Process Metallurgy and Materials Processing Science*, vol. **50**, no. 5, pp. 2088–94, 2019. DOI: 10.1007/s11663-019-01639-4
- Chen, Z., You, Y. and Morita, K., Exploration of Boron Removal from Molten Silicon by Introducing Oxygen Resources into Ammonia Blowing Treatment, *Canadian Metallurgical Quarterly*, vol. **58**, no. 1, pp. 82–88, 2019. DOI: 10.1080/00084433.2018.1507781
- Chin, C. H., Mebel, A. M. and Hwang, D. Y., Theoretical Study of the Reaction Mechanism of BO, B 2O 2, and BS with H 2, *Journal of Physical Chemistry A*, vol. **108**, no. 3, pp. 473–83, 2004. DOI: 10.1021/jp0357471
- Cox, J., Wagman, D. D. and Medvedev, V., *CODATA Key Values for Thermodynamics*, New York: Hemisphere publication, 1989.
- Dunning, T. H., Peterson, K. A. and Wilson, A. K., Gaussian Basis Sets for Use in Correlated Molecular Calculations. X. The Atoms Aluminum through Argon Revisited, *The Journal of Chemical Physics*, vol. **114**, no. 21, pp. 9244–53, June 2001. DOI: 10.1063/1.1367373
- Feller, D., Peterson, K. A. and Grant Hill, J., On the Effectiveness of CCSD(T) Complete Basis Set Extrapolations for Atomization Energies, *The Journal of Chemical Physics*, vol. **135**, no. 4, p. 044102, July 28, 2011. DOI: 10.1063/1.3613639
- Golewski, G. L. and Gil, D. M., Studies of Fracture Toughness in Concretes Containing Fly Ash and Silica Fume in the First 28 Days of Curing, *Materials*, vol. **14**, no. 2, pp. 1–21, 2021. DOI: 10.3390/ma14020319
- Hoseinpur, A. and Safarian, J., Mechanisms of Graphite Crucible Degradation in Contact with Si-Al

- Melts at High Temperatures and Vacuum Conditions, *Vacuum*, vol. **171**, p. 108993, January 2020. DOI: 10.1016/j.vacuum.2019.108993
- Hosseinpour, A. and Tafaghodi Khajavi, L., Phosphorus Removal from Si-Fe Alloy Using SiO2-Al2O3-CaO Slag, *Metallurgical and Materials Transactions B*, vol. **50**, no. 4, pp. 1773–81, August 24, 2019. DOI: 10.1007/s11663-019-01586-0
- Imler, W. R., Haun, R. E., Lampson, R. A., Charles, M. and Meese, P., Efficacy of Plasma Arc Treatment for the Reduction of Boron in the Refining of Solar-Grade Silicon, *Conference Record of the IEEE Photovoltaic Specialists Conference*, vol. **9718**, no. 1, pp. 003435–39, 2011. DOI: 10.1109/PVSC.2011.6186685
- IRENA, Future of Solar Photovoltaic: Deployment, Investment, Technology, Grid Integration and Socio-Economic Aspects, 2019.
- Jakobsson, L. K., Distribution of Boron between Silicon and CaO-SiO2 , MgO-SiO2 , CaO-MgO-SiO2 and CaO-Al2 O3 -SiO2 Slags at 1600° C, 2013.
- Jakobsson, L. K. and Tangstad, M., Thermodynamics of Boron Removal from Silicon Using CaO-MgO-Al2O3-SiO2 Slags, *Metallurgical and Materials Transactions B*, vol. **49**, no. 4, pp. 1699–1708, August 9, 2018. DOI: 10.1007/s11663-018-1250-7
- Jiang, W., Yu, W., Qin, H., Xue, Y., Li, C. and Lv, X., Boron Removal from Silicon by Hydrogen Assistant during the Electromagnetic Directional Solidification of Al Si Alloys, *International Journal of Hydrogen Energy*, vol. **44**, no. 26, pp. 13502–8, May 2019. DOI: 10.1016/j.ijhydene.2019.03.248
- Koria, S. C. and Lange, K. W., Penetrability of Impinging Gas Jets in Molten Steel Bath, *Steel Research*, vol. **58**, no. 9, pp. 421–26, 1987. DOI: 10.1002/srin.198700241
- Matthews, D. A., Cheng, L., Harding, M. E., Lipparini, F., Stopkowicz, S., Jagau, T.-C., Szalay, P. G., Gauss, J. and Stanton, J. F., Coupled-Cluster Techniques for Computational Chemistry: The <scp>CFOUR</Scp> Program Package, *The Journal of Chemical Physics*, vol. **152**, no. 21, p. 214108, June 7, 2020. DOI: 10.1063/5.0004837
- Muñoz-Esparza, D., Buchlin, J. M., Myrillas, K. and Berger, R., Numerical Investigation of Impinging Gas Jets onto Deformable Liquid Layers, *Applied Mathematical Modelling*, vol. **36**, no. 6, pp. 2687–2700, 2012. DOI: 10.1016/j.apm.2011.09.052
- Næss, M. K., Tranell, G., Olsen, J. E., Kamfjord, N. E. and Tang, K., Mechanisms and Kinetics of Liquid Silicon Oxidation During Industrial Refining, *Oxidation of Metals*, vol. **78**, no. 3–4, pp. 239–51, October 22, 2012. DOI: 10.1007/s11085-012-9303-9
- Nakamura, N., Baba, H., Sakaguchi, Y., Hiwasa, S. and Kato, Y., Boron Removal in Molten Silicon with Steam Added Plasma Melting Method, *Journal of the Japan Institute of Metals*, vol. **67**, no. 10, pp. 583–89, 2003. DOI: 10.2320/jinstmet1952.67.10_583
- Nguyen, A. V. and Evans, G. M., Computational Fluid Dynamics Modelling of Gas Jets Impinging onto Liquid Pools, *Applied Mathematical Modelling*, vol. **30**, no. 11, pp. 1472–84, 2006. DOI: 10.1016/j.apm.2006.03.015
- Nordstrand, E. F. and Tangstad, M., Removal of Boron from Silicon by Moist Hydrogen Gas, *Metallurgical and Materials Transactions B*, vol. **43**, no. 4, pp. 814–22, August 1, 2012. DOI: 10.1007/s11663-012-9671-1
- Philips, D. S., and Warmuth, W., Photovoltaics Report, *PSE Conferences and Consulting Gmbh*, Freiburg, 2019.
- Porter, R. F. and Gupta, S. K., Heats of Formation of Gaseous H 2 BOH and HB(OH) 2 1a, *The Journal of Physical Chemistry*, vol. **68**, no. 9, pp. 2732–33, September 1, 1964. DOI:

- 10.1021/j100791a511
- Raghunath, P., Lee, Y.-M., Wu, S.-Y., Wu, J.-S. and Lin, M.-C., Ab Initio Chemical Kinetics for Reactions of H Atoms with SiH x (x = 1-3) Radicals and Related Unimolecular Decomposition Processes, *International Journal of Quantum Chemistry*, vol. **113**, no. 12, pp. 1735–46, June 15, 2013. DOI: 10.1002/qua.24396
- Safarian, J., Thermochemical Aspects of Boron and Phosphorus Distribution Between Silicon and BaO-SiO2 and CaO-BaO-SiO2 Slags, *Silicon*, vol. **11**, no. 1, pp. 437–51, 2019. DOI: 10.1007/s12633-018-9919-8
- Safarian, J., Sanna, C., and Tranell, G., Boron Removal from Silicon by Moisturized Gases, *33rd European Photovoltaic Solar Energy Conference and Exhibition BORON*, vol. **2**, no. 7491, pp. 476–79, 2016.
- Safarian, J., Tang, K., Hildal, K. and Tranell, G., Boron Removal from Silicon by Humidified Gases, *Metallurgical and Materials Transactions E*, vol. **1**, no. 1, pp. 41–47, 2014. DOI: 10.1007/s40553-014-0007-8
- Safarian, J., Tang, K., Olsen, J. E., Andersson, S., Tranell, G. and Hildal, K., Mechanisms and Kinetics of Boron Removal from Silicon by Humidified Hydrogen, *Metallurgical and Materials Transactions B*, vol. **47**, no. 2, pp. 1063–79, April 29, 2016. DOI: 10.1007/s11663-015-0566-9
- Safarian, J. and Tangstad, M., Vacuum Refining of Molten Silicon, *Metallurgical and Materials Transactions B*, vol. **43**, no. 6, pp. 1427–45, December 26, 2012. DOI: 10.1007/s11663-012-9728-1
- Sakai, S. and Jordan, K. D., Structures and Vibrational Frequencies of HBeOH, HBOH, HCOH, HMgOH, HAlOH, and HSiOH, *Chemical Physics Letters*, vol. **130**, no. 1–2, pp. 103–10, 1986. DOI: 10.1016/0009-2614(86)80434-1
- Sortland, Ø. S. and Tangstad, M., Boron Removal from Silicon Melts by H2O / H2 Gas Blowing: Mass Transfer in Gas and Melt, *Metallurgical and Materials Transactions E*, vol. 1, no. 3, pp. 211–25, 2014. DOI: 10.1007/s40553-014-0021-x
- Standish, N., and He, Q. L., Drop Generation Due to an in the Steelmaking Vessel Impinging Jet and the Effect of Bottom Blowing, *ISIJ International*, 1989.
- Teixeira, L. A. V. and Morita, K., Removal of Boron from Molten Silicon Using CaO-SiO2 Based Slags, *ISIJ International*, vol. **49**, no. 6, pp. 783–87, 2009. DOI: 10.2355/isijinternational.49.783
- Thomas, S., Barati, M. and Morita, K., A Review of Slag Refining of Silicon Alloys, *Jom*, vol. **73**, no. 1, pp. 282–92, 2021. DOI: 10.1007/s11837-020-04474-0
- Vadon, M., Sortland, Ø., Tangstad, M., Chichignoud, G. and Delannoy, Y., Passivation Threshold for the Oxidation of Liquid Silicon and Thermodynamic Non-Equilibrium in the Gas Phase, *Metallurgical and Materials Transactions B*, vol. 49, no. 6, pp. 3330–42, December 17, 2018.
 DOI: 10.1007/s11663-018-1381-x
- Valiev, M., Bylaska, E. J., Govind, N., Kowalski, K., Straatsma, T. P., Dam, H. J. J. Van, Wang, D., et al., NWChem: A Comprehensive and Scalable Open-Source Solution for Large Scale Molecular Simulations, *Computer Physics Communications*, vol. 181, no. 9, pp. 1477–89, September 1, 2010. DOI: 10.1016/J.CPC.2010.04.018
- Vikan, H. and Justnes, H., Rheology of Cementitious Paste with Silica Fume or Limestone, *Cement and Concrete Research*, vol. **37**, no. 11, pp. 1512–17, November 2007. DOI: 10.1016/j.cemconres.2007.08.012
- Visuri, V.-V., Järvinen, M., Savolainen, J., Sulasalmi, P., Eetu-Pekka Heikkinen,) and Fabritius, T., A Mathematical Model for the Reduction Stage of the AOD Process. Part II: Model Validation

- and Results, *ISIJ International*, vol. **53**, no. 4, pp. 613–21, 2013. DOI: 10.2355/isijinternational.53.613
- Visuri, V.-V., Järvinen, M., Sulasalmi, P., Heikkinen, E.-P., Savolainen, J. and Fabritius, T., A Mathematical Model for the Reduction Stage of the AOD Process. Part I: Derivation of the Model, *ISIJ International*, vol. **53**, no. 4, pp. 603–12, 2013. DOI: 10.2355/isijinternational.53.603
- Wilson, G. M., Al-Jassim, M., Metzger, W. K., Glunz, S. W., Verlinden, P., Xiong, G., Mansfield, L. M., et al., The 2020 Photovoltaic Technologies Roadmap, *Journal of Physics D: Applied Physics*, vol. 53, no. 49, 2020. DOI: 10.1088/1361-6463/ab9c6a
- Wolf, K. J., Smeda, A., Müller, M. and Hilpert, K., Investigations on the Influence of Additives for SO2 Reduction during High Alkaline Biomass Combustion, *Energy and Fuels*, vol. **19**, no. 3, pp. 820–24, 2005. DOI: 10.1021/ef040081a
- WU, J. jun, MA, W. hui, YANG, B., DAI, Y. nian and MORITA, K., Boron Removal from Metallurgical Grade Silicon by Oxidizing Refining, *Transactions of Nonferrous Metals Society of China (English Edition)*, vol. **19**, no. 2, pp. 463–67, 2009. DOI: 10.1016/S1003-6326(08)60296-4
- Yang, D., *Handbook of Photovoltaic Silicon*, *Handbook of Photovoltaic Silicon*, Berlin, Heidelberg: Springer Berlin Heidelberg, pp. 1–841, 2019.
- Yvon, A., Fourmond, E., Ndzogha, C., Delannoy, Y., Trassy, C., Yvon, A., Fourmond, E., et al., Inductive Plasma Process for Refining of Solar Grade Silicon, *EPM 2003 4th International Conference on Electromag- Netic Processing of Materials*, pp. 125–30, 2011.
- Zhao, Y. and Truhlar, D. G., The M06 Suite of Density Functionals for Main Group Thermochemistry, Thermochemical Kinetics, Noncovalent Interactions, Excited States, and Transition Elements: Two New Functionals and Systematic Testing of Four M06-Class Functionals and 12 Other Function, *Theoretical Chemistry Accounts*, vol. **120**, no. 1–3, pp. 215–41, May 12, 2008. DOI: 10.1007/s00214-007-0310-x